

RESEARCH ARTICLE

10.1029/2018MS001412

This article is a companion to Ji and Yuan (2018) <https://doi.org/10.1029/2018MS001413>.

Key Points:

- CSSPv2 land model was developed over headwaters with conjunctive surface-subsurface flows, storage-based runoff, and soil organic matter
- CSSPv2 outperformed global reanalysis for simulations of hydrological cycle as validated with multisource observations
- CSSPv2 captured elevation-dependent warming, increasing ET and TWS in the satellite era, while global reanalysis failed over headwaters

Correspondence to:

X. Yuan,
yuanxing@tea.ac.cn

Citation:

Yuan, X., Ji, P., Wang, L., Liang, X.-Z., Yang, K., Ye, A., et al. (2018). High-resolution land surface modeling of hydrological changes over the Sanjiangyuan region in the eastern Tibetan plateau: 1. Model development and evaluation. *Journal of Advances in Modeling Earth Systems*, 10. <https://doi.org/10.1029/2018MS001412>

Received 18 JUN 2018
Accepted 10 OCT 2018
Accepted article online 15 OCT 2018

High-Resolution Land Surface Modeling of Hydrological Changes Over the Sanjiangyuan Region in the Eastern Tibetan Plateau: 1. Model Development and Evaluation

Xing Yuan^{1,2} , Peng Ji^{2,3}, Linying Wang², Xin-Zhong Liang⁴ , Kun Yang⁵ , Aizhong Ye⁶ , Zhongbo Su⁷ , and Jun Wen⁸

¹School of Hydrology and Water Resources, Nanjing University of Information Science and Technology, Nanjing, China, ²Key Laboratory of Regional Climate-Environment for Temperate East Asia, Institute of Atmospheric Physics, Chinese Academy of Sciences, Beijing, China, ³College of Earth and Planetary Sciences, University of Chinese Academy of Sciences, Beijing, China, ⁴Department of Atmospheric and Oceanic Science, and Earth System Science Interdisciplinary Center, University of Maryland, College Park, MD, USA, ⁵Ministry of Education Key Laboratory for Earth System Modeling, Department of Earth System Science, Tsinghua University, Beijing, China, ⁶State Key Laboratory of Earth Surface and Ecological Resources, Faculty of Geographical Science, Beijing Normal University, Beijing, China, ⁷Faculty of Geo-Information Science and Earth Observation, University of Twente, Enschede, Netherlands, ⁸Plateau Atmosphere and Environment Key Laboratory of Sichuan Province, College of Atmospheric Sciences, Chengdu University of Information Technology, Chengdu, China

Abstract High-resolution modeling became popular in recent years due to the availability of multisource observations, advances in understanding fine-scale processes, and improvements in computing facilities. However, modeling of hydrological changes over mountainous regions is still a great challenge due to the sensitivity of highland water cycle to global warming, tightly coupled hydrothermal processes, and limited observations. Here we show a successful high-resolution (3 km) land surface modeling over the Sanjiangyuan region located in the eastern Tibetan plateau, which is the headwater of three major Asian rivers. By developing a new version of a Conjunctive Surface-Subsurface Process model named as CSSPv2, we increased Nash-Sutcliffe efficiency by 62–130% for streamflow simulations due to the introduction of a storage-based runoff generation scheme, reduced errors by up to 31% for soil moisture modeling after considering the effect of soil organic matter on porosity and hydraulic conductivity. Compared with ERA-Interim and Global Land Data Assimilation System version 1.0 reanalysis products, CSSPv2 reduced errors by up to 30%, 69%, 92%, and 40% for soil moisture, soil temperature, evapotranspiration, and terrestrial water storage change, respectively, as evaluated against in situ and satellite observations. Moreover, CSSPv2 well captured the elevation-dependent ground temperature warming trends and the decreased frozen dates during 1979–2014, and significant increasing trends ($p < 0.05$) in evapotranspiration and terrestrial water storage during 1982–2011 and 2003–2014 respectively, while ERA-Interim and Global Land Data Assimilation System version 1.0 showed no trends or even negative trends. This study implies the necessity of developing high-resolution land surface models in realistically representing hydrological changes over highland areas that are sentinels to climate change.

1. Introduction

Climate change influences Earth's energy cycle through altering cloud distributions and atmospheric radiation, and consequently affects terrestrial water cycle. In a warming climate, the increases in precipitable water and evapotranspiration (ET) result in higher chance for floods and droughts (Dai, 2013; Milly et al., 2002). The fifth Assessment Report of the Intergovernmental Panel on Climate Change suggests that heavy precipitation events are very likely to increase over most of the midlatitude regions and wet tropical regions, and the intensity and duration of droughts are likely to increase over presently dry regions (Intergovernmental Panel on Climate Change, 2013). The changing climate and the increasing risk of extremes impose an urgent need to assess the changes in terrestrial hydrology for water and food security, as well as for a sustainable management of the environment. However, there are great challenges in simulating and projecting the hydrological cycle and extremes (Prudhomme et al., 2014) due to the uncertainty in land surface models (LSMs), especially over mountainous areas that are the sentinels of climate change.

©2018. The Authors.
This is an open access article under the terms of the Creative Commons Attribution-NonCommercial-NoDerivs License, which permits use and distribution in any medium, provided the original work is properly cited, the use is non-commercial and no modifications or adaptations are made.

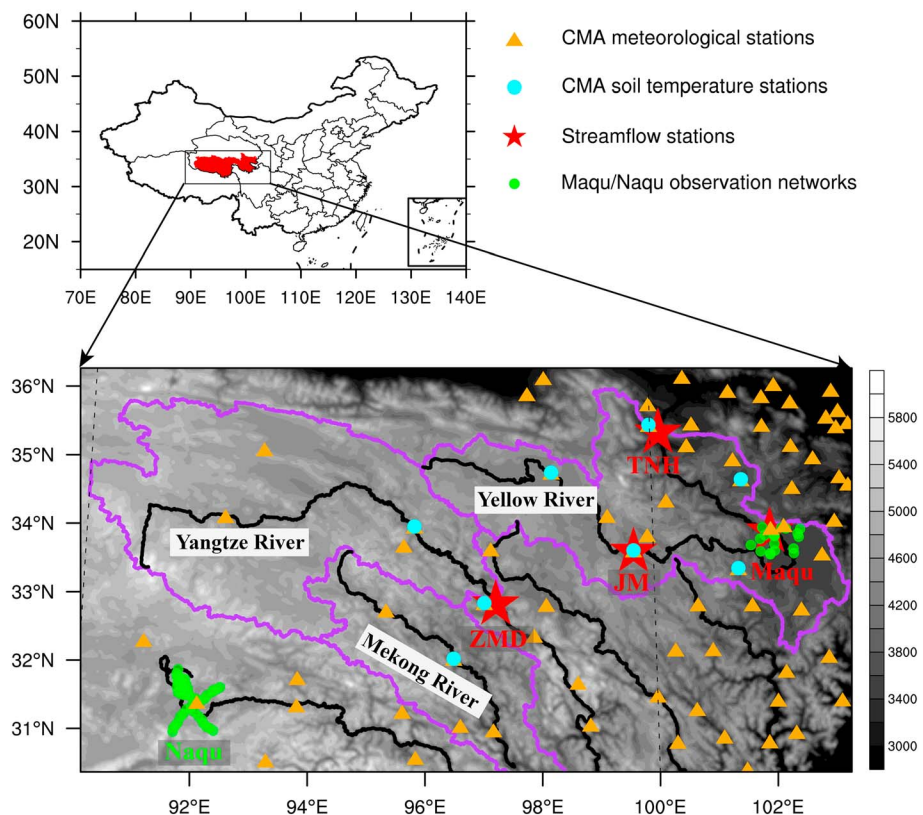


Figure 1. Study domain and observational station locations over the Sanjiangyuan region. Shaded is topography. Orange triangles represent China Meteorological Administration (CMA) stations, and cyan dots are those stations where monthly soil temperature observations are provided. Four hydrological stations with monthly streamflow and two observation networks with daily soil moisture and soil temperature are shown by red pentagrams and green dots, respectively. Headwaters of the Yellow River basin, the Yangtze River basin, and the Lancang-Mekong River basin are shown by purple lines, with black lines showing main channels.

Through five decades of development, LSMs have been augmented from simple bucket models (Manabe, 1969) to comprehensive Earth system models that simulate water cycle, energy cycle, carbon cycle, and even nutrient cycle (Oleson et al., 2013; Tian et al., 2016). Besides developing a very complicated system that is expected to consider as many biogeophysical and biogeochemical processes as possible, another direction is to make LSMs useful for applications (Wood et al., 2011), for example, water resources management (Wada et al., 2014), flood/drought early warning (Wing et al., 2017), and detection and attribution of hydrological changes (Yuan et al., 2018). The latter direction requires developing high-resolution LSMs that can provide locally relevant information (Bierkens et al., 2015). As LSMs go into high or even hyper resolution (Wood et al., 2011), many hydrological processes that are neglected in coarse resolution Earth system models may have significant influence on the simulations (Melsen et al., 2016), such as the lateral flows, overland flow, ponding, and surface-subsurface interactions (Ji et al., 2017; Maxwell & Condon, 2016; Niu et al., 2014).

For the mountainous region, phenomena including snowmelt runoff (Cuo et al., 2013), frozen soil (Li et al., 2012), effects of organic matters and minerals on soil hydrothermal dynamics (Chen et al., 2012), and elevation-dependent warming (Pepin et al., 2015) make the land surface modeling more difficult especially in a changing climate. In addition, the resolution of meteorological forcings and land surface data is also critical for a successful simulation (Ji et al., 2017; Wood et al., 2011). This would be a challenge for the modeling of terrestrial hydrology over mountainous regions due to sparse in situ measurements, as well as large uncertainty in radar and satellite retrievals.

Located in the eastern part of the Tibetan plateau (TP; Figure 1), the Sanjiangyuan region is the headwaters of the Yellow River, the Yangtze River, and the Lancang-Mekong River. The Sanjiangyuan region is called as the *China Water Tower* because it provides resources for the freshwater supply, hydropower, industry,

agricultural, and environment sustainability over downstream areas. A warming and drying climate during 1980s–1990s, combined with intensive adverse human activities, resulted in a decrease in water resources, grassland degradation, and even desertification. Since the beginning of the 21st century, China has launched the *Sanjiangyuan Region Reserve* project, including the *Graze for Grass*, ecological migration, etc. After the environment protection for several years, the Sanjiangyuan region is experiencing an increase in the areas of grassland and lake, and an increase in the streamflow. Meanwhile, the drying climate also switched to a wetting climate at the beginning of the 21st century (Jiang & Zhang, 2016; Liu et al., 2014). Therefore, whether the climate change or the land cover change has more significant influence on the hydrological changes over the Sanjiangyuan region remains unknown.

As the first paper of a two-part series, this paper introduces a high-resolution LSM developed over the Sanjiangyuan region and validates it with multisource observations including streamflow observations at hydrological gauges over the headwaters region, in situ soil moisture and soil temperature measurements from two densely distributed networks, and ET and terrestrial water storage estimations from satellite data. Specifically, we not only assess the model's performance in terms of simulating hydrological variations from daily to monthly time scales but also evaluate its ability in capturing long-term changes in the terrestrial hydrology over the Sanjiangyuan region. Building upon the confidence of the high-resolution land surface modeling, attribution of the changes in the hydrological cycle with respect to anthropogenic and natural climate change, and land cover change, will be illustrated in a companion paper, using LSM simulations driven by a set of Coupled Model Intercomparison Project phase 5 models under different forcings (Ji & Yuan, 2018).

2. Model, Data, and Experimental Design

2.1. The Conjunctive Surface-Subsurface Process Model

The LSM used in this study is the Conjunctive Surface-Subsurface Process (CSSP) model (Ji et al., 2017; Liang et al., 2012; Yuan & Liang, 2011). The CSSP model was developed from the Common Land Model (Dai et al., 2003, 2004), but it has better representations in lateral surface and subsurface hydrological processes and their interactions (Choi et al., 2013). Generally, CSSP model includes a quasi-three-dimensional subsurface soil water transport model (Choi et al., 2007), a one-dimensional diffusive surface water model (Choi, 2006), and a one-dimensional groundwater model (Yuan & Liang, 2011). The lateral surface and subsurface flows were found to be nontrivial for high-resolution land surface modeling (Ji et al., 2017).

The runoff generation in the CSSP model includes surface and subsurface runoff (Choi & Liang, 2010; Yuan & Liang, 2011). Surface runoff (R_s , mm/s) is calculated as the sum of Hortonian (rainfall rate exceeds infiltration rate) and Dunnian (rainfall occurs at saturated area) runoff:

$$R_s = (1 - F_{\text{imp}}) \max[0, Q_w - I_{\text{max}}] + F_{\text{imp}} Q_w, \quad (1)$$

where F_{imp} is the impermeable area fraction that includes saturated and frozen parts, Q_w (mm/s) is the total available water supply rate that consists of rainfall, dewfall, and snowmelt rates. The I_{max} (mm/s) is the maximum infiltration rate defined as

$$I_{\text{max}} = F_{\text{liq}}(1) K_{\text{sz}}(1) \left[1 + \frac{\psi_s(1) b_1}{d_1} (w_u(1) - 1) \right], \quad (2)$$

where the index (1) means the top soil layer and F_{liq} is the unfrozen parts. K_{sz} (mm/s) and ψ_s (mm) represent the saturated hydraulic conductivity and saturated suction head, respectively. The w_u is the soil wetness for the permeable unsaturated area, and b_1 is pore size distribution index, which is determined by soil clay content. The node depth of top layer is denoted by d_1 (mm). The CSSP model predicts subsurface runoff as the sum of saturation excess, baseflow, and bottom drainage. The saturation excess runoff is calculated by removing supersaturated water from the entire soil column. Baseflow ($R_{\text{sb, lat}}$, mm/s) calculation is the water table-based scheme proposed by Niu et al. (2005):

$$R_{\text{sb, lat}} = R_{\text{sb, max}} e^{-f z_v}, \quad (3)$$

where $R_{\text{sb, max}} = 4.5 \times 10^{-3}$ mm/s is the maximum subsurface lateral runoff and f is the exponential decay factor. The z_v (m) represents water table depth. $R_{\text{sb, lat}}$ is extracted from each saturated layer in proportion to its local hydraulic conductivity without exceeding the available liquid water mass. The bottom drainage

was dropped in this study because of the consideration of recharge rate between the lowest soil layer and the unconfined aquifer (Yuan & Liang, 2011). The river transport model (Oleson et al., 2013), which is similar to the linear reservoir model, was used to route surface and subsurface runoff from each grid cell to its downstream neighboring grid cell, where water flow velocity and river water stored within the grid cell were used to calculate the flux of water leaving the grid cell.

2.2. CSSP Model Development

In order to reasonably simulate energy and water cycle over headwater region, we have updated the CSSP model in a few aspects, including the runoff generation, soil organic matter and thermal parameterizations, and dynamical memory allocation suitable for high-resolution simulations. The new model is named as CSSP version 2 (CSSPv2).

2.2.1. Incorporating the Storage-Based Runoff Scheme

For runoff generation, Zheng et al. (2017) compared four different schemes over upper Yellow River in the TP and found soil water storage-based runoff parameterizations outperformed water table-based runoff schemes for the seasonally frozen and high-altitude rivers. Thus, we incorporated the Variable Infiltration Capacity (Liang et al., 1994) runoff parameterization into CSSP following Oleson et al. (2013). The saturated area fraction in CSSPv2 is now parameterized as

$$f_{\text{sat}} = 1 - (1 - w_{\text{top}}/w_{s,\text{top}})^{1/(1+b)}, \quad (4)$$

where w_{top} (mm) and $w_{s,\text{top}}$ (mm) are the sum of actual and saturated soil water for the upper six soil layers, respectively. The parameter b determines the shape of infiltration curve. The actual (i , mm) and saturated (i_m , mm) soil moisture holding capacity of each grid cell are calculated as

$$\begin{aligned} i &= i_m \left(1 - (1 - f_{\text{sat}})^{1/b} \right) \\ i_m &= w_{s,\text{top}}(1 + b), \end{aligned} \quad (5)$$

and the maximum soil infiltration rate becomes

$$I_{\text{max}} = \begin{cases} (w_{s,\text{top}} - w_{\text{top}})/\Delta t & i + Q_w \Delta t \geq i_m \\ (w_{s,\text{top}} - w_{\text{top}}) - w_{s,\text{top}} \times \left[1 - \max\left(1, \frac{i + Q_w \Delta t}{i_m}\right)^{1+b} \right] / \Delta t & i + Q_w \Delta t < i_m \end{cases}, \quad (6)$$

The baseflow is parameterized as

$$R_{s,\text{lat}} = \left[\frac{D_s D_{s,\text{max}}}{w_s w_{s,\text{bot}}} w_{\text{bot}} + \max\left(0, \frac{w_{\text{bot}} - w_s w_{s,\text{bot}}}{w_{s,\text{bot}} - w_s w_{s,\text{bot}}}\right) \left(D_{s,\text{max}} - \frac{D_s D_{s,\text{max}}}{w_s} \right) \right], \quad (7)$$

where $D_{s,\text{max}}$ (mm/s) is the maximum subsurface flow rate, D_s is a fraction of $D_{s,\text{max}}$, w_{bot} (mm) and $w_{s,\text{bot}}$ (mm) are actual and maximum soil water content for 7–9 soil layers, and w_s is a fraction of $w_{s,\text{bot}}$.

2.2.2. Considering the Soil Organic Matter in Soil Hydraulic Properties

Considering the high soil organic content for the alpine grassland, CSSPv2 uses parameterizations for hydraulic properties as follows (Oleson et al., 2013):

$$\begin{aligned} \theta_{s,i} &= (1 - f_{\text{om},i})\theta_{s,\text{min},i} + f_{\text{om},i}\theta_{s,\text{om}} \\ B_i &= (1 - f_{\text{om},i})B_{\text{min},i} + f_{\text{om},i}B_{\text{om}} \\ \psi_{s,i} &= (1 - f_{\text{om},i})\psi_{s,\text{min},i} + f_{\text{om},i}\psi_{s,\text{om}}, \end{aligned} \quad (8)$$

where the index i represents a specific soil layer and $\theta_{s,i}$, $\theta_{s,\text{min},i}$, and $\theta_{s,\text{om}}$ are mean porosities for actual soil, pure mineral soil, and organic matter. The $f_{\text{om},i}$ means soil organic matter fraction, B_i is a parameter that will be used in hydraulic conductivity, and $\psi_{s,i}$ (m) is a saturated soil suction head.

2.2.3. Introducing a Modified Soil Thermal Parameterization

CSSP calculates soil thermal conductivity (λ , $\text{W}\cdot\text{m}^{-1}\cdot\text{K}^{-1}$) as

$$\lambda = K_e(\lambda_{\text{sat}} - \lambda_{\text{dry}}) + \lambda_{\text{dry}}, \quad (9)$$

where λ_{sat} ($\text{W}\cdot\text{m}^{-1}\cdot\text{K}^{-1}$) and λ_{dry} ($\text{W}\cdot\text{m}^{-1}\cdot\text{K}^{-1}$) are the saturated and dry thermal conductivity, respectively, and K_e is the Kersten number, which is a function of soil wetness (S_r) and the phase of the water:

$$K_e = \begin{cases} \log(S_r) + 1, & \text{unfrozen soils} \\ S_r, & \text{frozen soils} \end{cases}. \quad (10)$$

The saturated thermal conductivity (λ_{sat}) is a combination of mineral (λ_m , $\text{W}\cdot\text{m}^{-1}\cdot\text{K}^{-1}$), ice (λ_{ice} , $\text{W}\cdot\text{m}^{-1}\cdot\text{K}^{-1}$), and water (λ_w , $\text{W}\cdot\text{m}^{-1}\cdot\text{K}^{-1}$) conductivity:

$$\lambda_{\text{sat}} = \lambda_m^{1-F_{\text{liq}}-F_{\text{ice}}} \lambda_{\text{ice}}^{F_{\text{ice}}} \lambda_w^{F_{\text{liq}}}, \quad (11)$$

where F_{ice} and F_{liq} are the frozen and liquid volume fractions, respectively. The mineral conductivity is determined by soil sand (%sand) and clay (%clay) fractions as

$$\lambda_m = \frac{8.8(\% \text{ sand}) + 2.92(\% \text{ clay})}{(\% \text{ sand}) + (\% \text{ clay})}. \quad (12)$$

Chen et al. (2012) compared the performance of three different soil thermal conductivity schemes in four alpine grassland stations and found that they overestimated thermal conductivity, but the scheme from Yang et al. (2005) outperformed others. Following Yang et al. (2005), parameterizations for λ_m and K_e in CSSPv2 are now as follows:

$$K_e = \begin{cases} \lambda_m = \lambda_q^q \lambda_o^{1-q} \\ \exp[k_T(1 - 1/S_r)], & \text{unfrozen soils} \\ S_r, & \text{frozen soils} \end{cases}, \quad (13)$$

where λ_m is determined by thermal conductivity of the quartz content (λ_q , $\text{W}\cdot\text{m}^{-1}\cdot\text{K}^{-1}$) and other minerals (λ_o , $\text{W}\cdot\text{m}^{-1}\cdot\text{K}^{-1}$), and K_e is expressed as an exponential form. Following Chen et al. (2012), the quartz content (q) was estimated as a half of sand fraction.

2.3. Study Area and Validation Data

In this study, we implemented the CSSPv2 model over the Sanjiangyuan region (Figure 1), which covers $31^\circ29'N$ – $36^\circ12'N$ and $90^\circ36'E$ – $103^\circ24'E$, with a total area of about $28.1 \times 10^4 \text{ km}^2$. It is mainly controlled by East Asian monsoon in summer and westerlies in winter (Yang et al., 2014). The eastern part has a relatively warmer and wetter climate with about 770-mm annual precipitation and 4.2°C mean temperature, while the western part is cold and arid where the annual precipitation and temperature are only 260 mm and -5.4°C , respectively (Xu et al., 2011). As a result, the eastern and southeastern parts are dominated by grassland and the northwestern part is barren or sparsely vegetated.

Daily ground temperature (TG) observations from 73 China Meteorological Administration (CMA) stations (orange triangles in Figure 1) were collected in this study, with eight stations including daily soil temperature observations at depths of 5, 10, 15, 20, and 40 cm (cyan dots in Figure 1). These temperature observations were averaged into monthly means. Monthly streamflow from four hydrological stations (red pentagrams in Figure 1), including the Jimai (JM), Maqu, Tangnaihai (TNH) stations in the Yellow River, and the Zhimenda (ZMD) station in the Yangtze River, was provided by the local authorities (Yuan et al., 2017). Data periods are 1979–2001 for the JM and Maqu stations, 1979–2010 for the TNH station, and 1980–2008 for the ZMD station.

Two soil temperature and soil moisture observation networks (Figure 1) are located in the study domain (Su et al., 2013; Yang et al., 2013). They were widely used in studies for hydrological cycle over TP (Bi et al., 2016;

Chen et al., 2013; Dente et al., 2012; Qin et al., 2013; Zeng et al., 2016). Lying in the east of the study domain, the Maqu network consists of 20 stations with soil moisture and soil temperature measurements from the depths of 5 to 80 cm, recorded every 15 min during 13 May 2008 to 29 June 2012 (Su et al., 2013). These stations are distributed in the valley of Yellow River headwaters and its surrounding hills, with main vegetation types being woodland and grassland. Climate in the Maqu network is featured by a humid and warm summer and a dry and cold winter. The Naqu network is located at the southwestern part of the study area where the climate is arid and cold. Fifty-six stations were set up in the Naqu network at three spatial scales (1.0° , 0.3° , and 0.1°) to observe soil moisture and soil temperature from the depths of 5 to 40 cm every 30 min from 2 August 2010 to 31 December 2014. As the highest soil moisture observation network above sea level in the world, elevations of the Naqu network vary from 4,470 to 4,950 m and the terrain is relatively smooth with rolling hummocks and hills (Yang et al., 2013). Alpine grassland is the main vegetation for the Naqu network. Both Maqu and Naqu networks have a typical freeze-thaw cycle, and only the liquid water can be observed.

The ET is a vital variable in the hydrological cycle and the climate system (Jung et al., 2010). Although tremendous progresses have been made in extending ET observations globally, they are limited over TP. Here the ensemble mean of Model Tree Ensemble evapotranspiration (MTE_ET; Jung et al., 2009) and the Global Land Evaporation Amsterdam Model evapotranspiration (GLEAM_ET; Miralles et al., 2011) version 3.1a was used. The MTE_ET data set was developed by using a machine-learning algorithm that integrated ET measurements at the FLUXNET stations (Baldocchi et al., 2001) to spatial grids according to surface meteorological data and remote sensed geospatial information (Jung et al., 2009). This data-driven estimation was validated by using flux tower observations, simulations from 16 LSMs and ET estimated from 112 catchments based on the water balance approach, and the MTE_ET estimations were quite satisfactory (Jung et al., 2010). The resolution of the MTE_ET data is $0.5^\circ \times 0.5^\circ$, and the data coverage is 1982–2011 (<https://www.bgc-jena.mpg.de/geodb/projects/Data.php>). For the GLEAM_ET data, observed precipitation and reanalysis data were first used to calculate potential ET. Then, a vegetation fraction-dependent, multiplicative stress index was used to convert potential ET into actual ET (Martens et al., 2017). The resolution of GLEAM_ET is $0.25^\circ \times 0.25^\circ$, and the data coverage is from 1980 to present (<https://www.gleam.eu/#datasets>). Both the MTE_ET and GLEAM_ET products were first interpolated into 3-km resolution through the inverse distance weighting interpolation method, and an ensemble of them was then calculated during 1982–2011.

The Gravity Recovery and Climate Experiment (GRACE) satellite provides a reliable estimation for the terrestrial water storage change (TWSC, Landerer & Swenson, 2012). There are three different processing centers releasing monthly GRACE data including the Geoforschungs Zentrum Potsdam, the Center for Space Research at University of Texas, Austin, and the Jet Propulsion Laboratory. These three data centers used different solutions when processing the GRACE TWS anomaly data, and the ensemble of them was suggested by the National Aeronautics and Space Administration (<https://grace.jpl.nasa.gov/data/choosing-a-solution/>). For more details, readers are kindly referred to the website (ftp://podaac-ftp.jpl.nasa.gov/allData/tellus/L3/land_mass/RL05/).

Besides validating CSSPv2 by comparing with multisource observations, simulations from Global Land Data Assimilation System version 1.0 (GLDAS1) reanalysis data (Rodell et al., 2004) and European Center for Medium-Range Weather Forecasts Interim Re-Analysis (ERA-Interim, Dee et al., 2011) were also used for model intercomparisons. GLDAS1 provides data at $1^\circ \times 1^\circ$ resolution at 3-hourly time scale, and ERA-Interim provides products at $0.75^\circ \times 0.75^\circ$ resolution at daily scale.

2.4. Experimental Design

In this paper, both the CSSP and CSSPv2 models were run at 3-km resolution over the Sanjiangyuan region (Figure 1) with 420×220 grid points generated from the Lambert map projection centered at (33.5°N , 96.7°E). All simulations were conducted for two cycles from 1979 to 2014 at half-hourly time step, with the land surface conditions at the end of the first cycle being used for the initial conditions for the simulations in the second cycle. So the simulations in the first cycle were regarded as model spin-up for a more stable initial conditions, and the results in the second cycle were used for analysis.

The digital elevation model data at 90-m resolution was obtained from U.S. Geological Survey website (<http://hydrosheds.cr.usgs.gov>) to calculate topographic characteristics (e.g., slopes and their standard deviations) for the CSSP and CSSPv2 model simulations. The slopes were used to compute terrain-driven lateral

Table 1
Performance for Streamflow Simulations Assessed at Four Hydrological Stations Over the Sanjiangyuan Region

Periods	CC		NSE		KGE		
	CSSP	CSSPv2	CSSP	CSSPv2	CSSP	CSSPv2	
TNH	Calibration (2000–2010)	0.83	0.95	0.55	0.89	0.74	0.88
	Validation (1979–1999)	0.80	0.93	0.52	0.84	0.74	0.82
ZMD	Calibration (2000–2008)	0.68	0.95	0.41	0.83	0.65	0.77
	Validation (1980–1999)	0.62	0.93	0.37	0.84	0.56	0.88
JM	Validation (1979–2001)	0.80	0.89	0.31	0.70	0.50	0.76
Maqu	Validation (1979–2001)	0.83	0.93	0.37	0.85	0.56	0.88

Note. The metrics include correlation coefficient (CC), Nash-Sutcliffe efficiency (NSE), and Kling-Gupta efficiency (KGE, Gupta et al., 2009). CSSP = Conjunctive Surface-Subsurface Process; CSSPv2 = Conjunctive Surface-Subsurface Process version 2; JM = Jimai; TNH = Tangnaihai; ZMD = Zhimenda.

surface and subsurface flows, while the standard deviations were used to derive the covariance between soil moisture and terrain slopes (Choi et al., 2007). High-resolution (1 km) land surface data sets including soil sand, clay, and organic matter fractions were provided by Dai et al. (2013). Normalized Difference Vegetation Index (NDVI) from the Global Inventory Modeling and Mapping Studies (GIMMS) at 8-km resolution during 1982–2000 (Pinzon & Tucker, 2014) and the Moderate Resolution Imaging

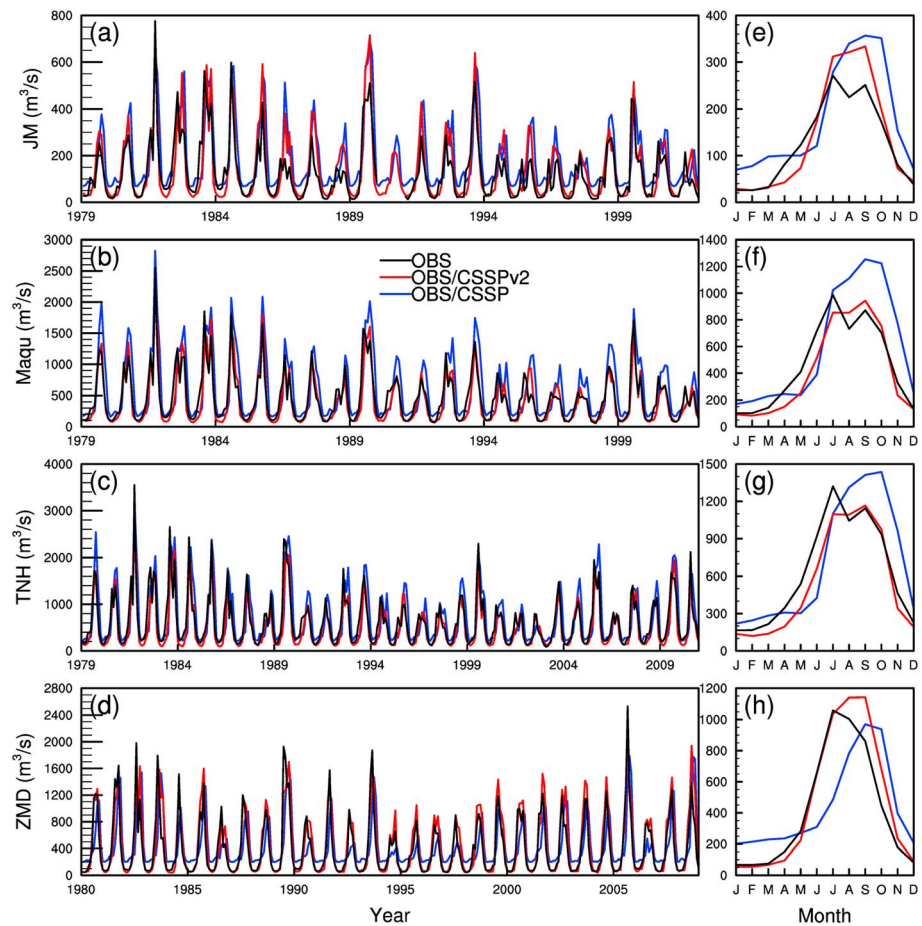


Figure 2. Observed and simulated monthly streamflow (a–d) and their annual cycles (e–h) at Jimai (JM), Maqu, Tangnaihai (TNH), and Zhimenda (ZMD) hydrological stations. Black lines are observations; blue and red lines are simulations by CSSP and CSSPv2, respectively. CSSP = Conjunctive Surface-Subsurface Process; CSSPv2 = Conjunctive Surface-Subsurface Process version 2.

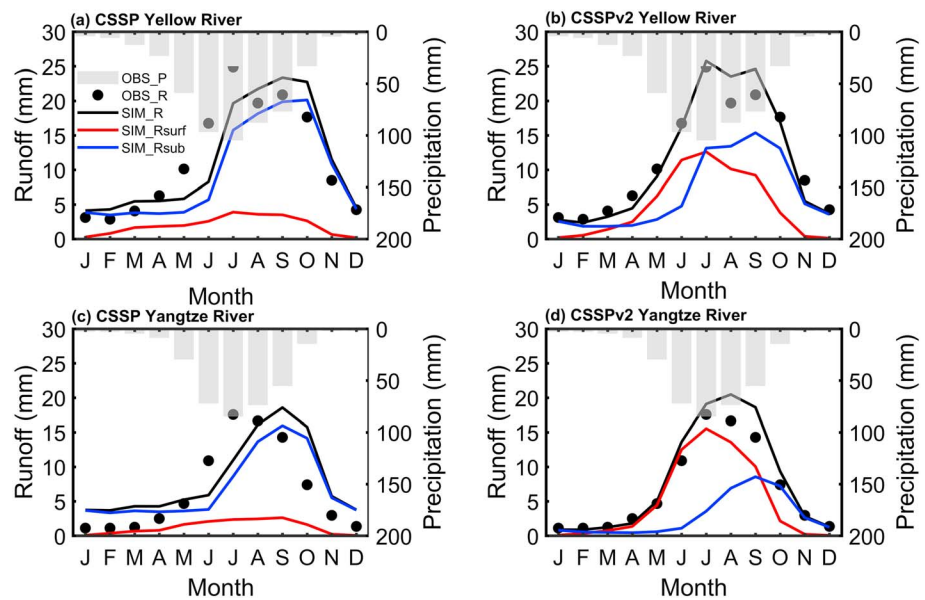


Figure 3. Observed and simulated climatology of runoff (mm; dots and lines), and observed climatology of precipitation (OBS_P, mm; gray bars) averaged over the headwaters of Yellow River and Yangtze River. OBS_R, SIM_R, SIM_Rsurf, and SIM_Rsub represent observed total runoff, simulated total runoff, simulated surface runoff, and simulated subsurface runoff, respectively. CSSP = Conjunctive Surface-Subsurface Process; CSSPv2 = Conjunctive Surface-Subsurface Process version 2.

Spectroradiometer (MODIS) at 0.05° resolution during 2001–2014 (LP-DACC, 2007) were merged. This is because MODIS data have a higher resolution, and Zhang et al. (2013) suggested that GIMMS NDVI data may be unreasonable during 2001–2006. Indeed, we compared the NDVI trends for the GIMMS, the MODIS, and the Système Pour l’Observation de la Terre VEGETATION (SPOT-VGT) during 2000–2014 and found that the GIMMS NDVI showed a decreasing trend, but MODIS NDVI and SPOT-VGT NDVI increased significantly. Dynamic leaf area index was derived from the merged NDVI using an empirical transformation (Sellers et al., 1996) and was used to provide surface conditions for the simulations. The land use data were compiled from the MODIS data at 1-km resolution.

The 0.1° China Meteorological Forcing Dataset (CMFD) from 1979 to 2014 with a 3-hourly temporal resolution (He & Yang, 2011) was used to generate forcing data over the study domain. The CMFD was produced by merging a variety of data sources, including observations from 740 CMA meteorological stations, Tropical Rainfall Measuring Mission satellite precipitation analysis data, GLDAS forcing data, Global Energy and Water Cycle Experiment-Surface Radiation Budget downward shortwave radiation, and the Princeton forcing data. Given that CMFD precipitation and temperature were based on 740 station observations, they were replaced by updated observations from 2,474 CMA stations (Wang et al., 2016) in this study. All the forcing data sets were bilinearly interpolated into 3-km resolution and disaggregated into half-hourly time step.

3. Validation of CSSPv2 Over the Sanjiangyuan Region

As the first part of a series investigating hydrological changes over the Sanjiangyuan region, this paper comprehensively evaluated the newly developed CSSPv2 model by comparing with its previous version CSSP, as well as global reanalysis for the simulations of streamflow, soil moisture, soil temperature, ET, and TWSC.

3.1. Streamflow

The CSSPv2 model was calibrated manually against monthly streamflow observations at TNH and ZMD stations (Figure 1) for the headwaters of Yellow River and Yangtze River, respectively, using the Nash-Sutcliffe efficiency (NSE) as the objective function. The CSSP model was minimally calibrated by Yuan and Liang (2011) over the United States, so the CSSPv2 model was also minimally calibrated (i.e., through a few sensitivity tests) for the streamflow simulations to allow for a consistent implementation of runoff generation

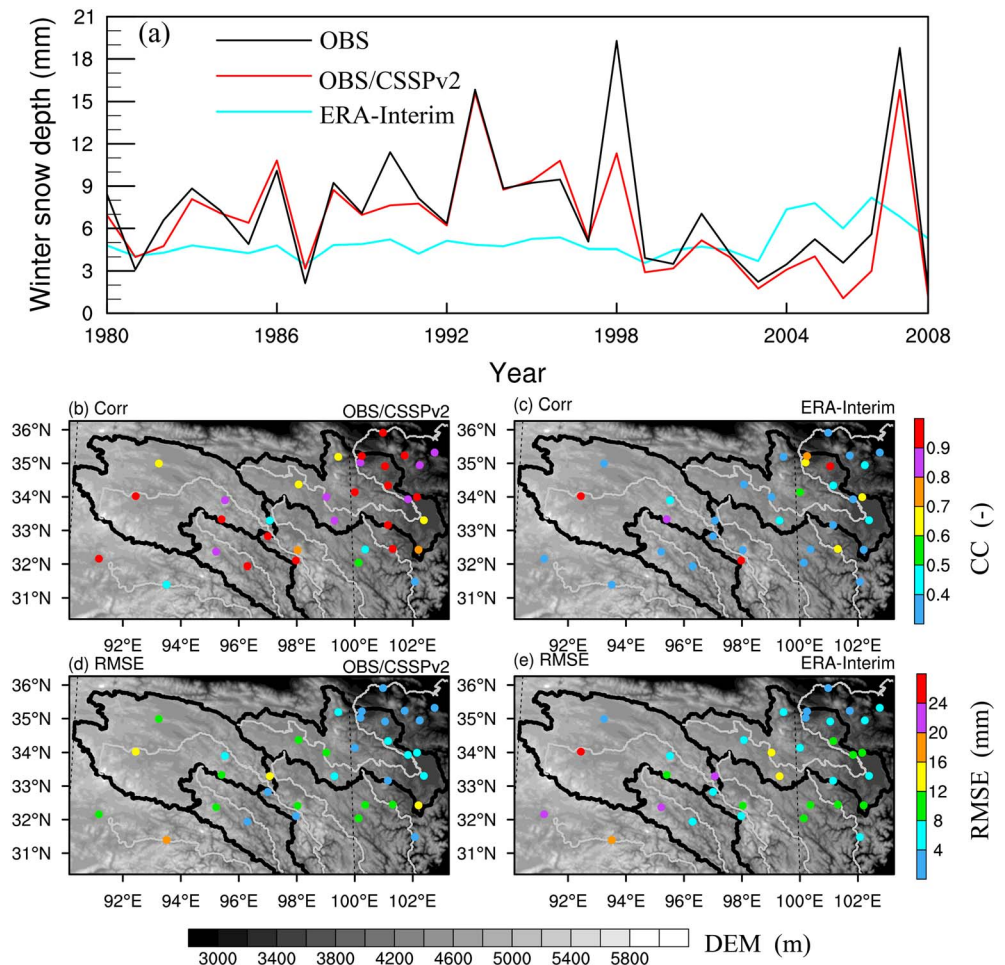


Figure 4. Evaluation of snow depth simulations over the Sanjiangyuan region. (a) Time series of observed and simulated December-January-February (DJF) mean snow depths averaged over 34 CMA stations. (b–e) Correlations and root-mean-square errors calculated over each CMA stations with snow depth observations. RMSE = root-mean-square error; CSSPv2 = Conjunctive Surface-Subsurface Process version 2; CMA = China Meteorological Administration.

schemes with other physical parameterizations. Except for the soil layer depths (Yuan et al., 2016) that were fixed for the CSSPv2 model, the variable infiltration curve parameter b , maximum baseflow velocity D_{smax} , fraction of D_{smax} where nonlinear baseflow begins (D_s), and fraction of maximum soil moisture content above which nonlinear baseflow occurs (w_s) were calibrated. Table 1 lists the calibration and validation periods. Sanjiangyuan region experienced significant land cover change during the period 2000–2010, so it was selected as the calibration period to fully capture the effects of land cover change on terrestrial hydrology besides streamflow (e.g., ET and TWSC). The years 1979–1999 were selected as validation period for streamflow simulations. For the JM and Maqu gauges (Figure 1) within the headwaters of the Yellow River, the results can be regarded as validation given no direct calibration against their streamflow records. Again, this treatment is to allow for a fair comparison with the CSSP model to the extent possible.

Figure 2 shows that CSSPv2 simulations captured the observed streamflow variations reasonably well at four stations, while CSSP overestimated streamflow especially during dry seasons. For the seasonal variations, double peaks that occurred in July and September at Maqu and TNH stations were also roughly captured by CSSPv2, while CSSP only simulated a peak streamflow during September (Figures 2f and 2g). For the ZMD station at the headwaters of the Yangtze River, CSSP failed to capture the timing of the peak streamflow, while CSSPv2 performed well (Figure 2h). The difference in streamflow seasonal cycle between CSSP and CSSPv2 was caused by the partitioning of surface and subsurface runoff (Figure 3). For the Yellow River

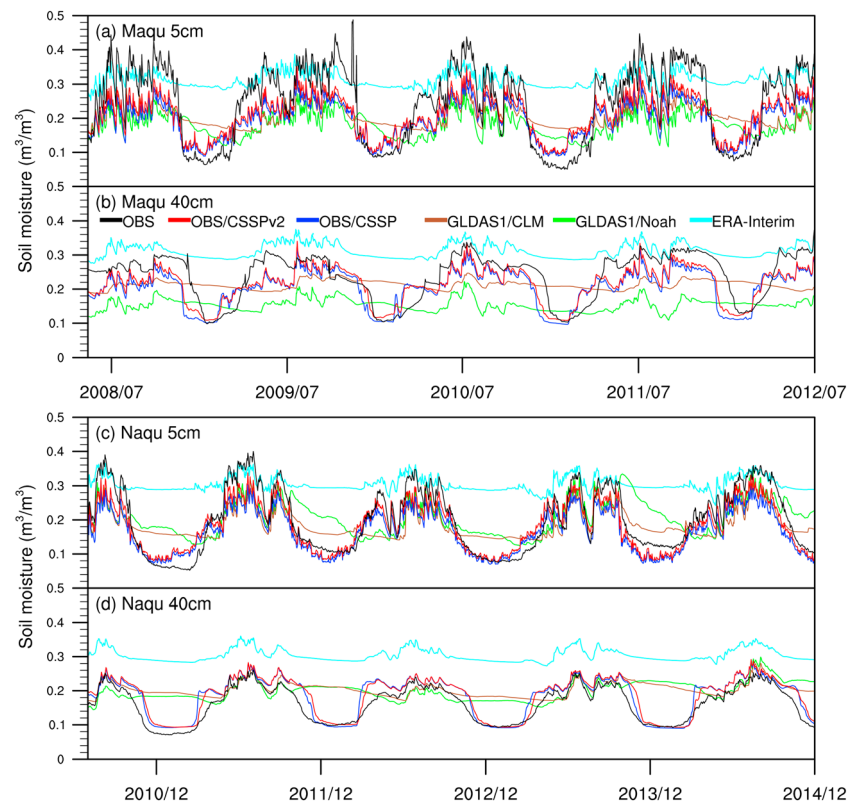


Figure 5. Observed and simulated daily soil moisture (m^3/m^3) averaged over Maqu and Naqu regions at the depths of 5 and 40 cm. Black lines are observations; blue and red lines are simulations from CSSP and CSSPv2. Simulations from GLDAS1/CLM, GLDAS1/Noah, and ERA-Interim reanalysis data sets are also shown by brown, green, and cyan lines. CSSP = Conjunctive Surface-Subsurface Process; CSSPv2 = Conjunctive Surface-Subsurface Process version 2; CLM = Community Land Model; GLDAS = Global Land Data Assimilation System.

headwater region, it is found that subsurface runoff dominates the total runoff for CSSP (blue line in Figure 3a), while both surface and subsurface runoff are important for CSSPv2 (Figure 3b). For the double peaks in annual cycle (Figures 2e–2g), CSSPv2 simulation shows that both surface and subsurface runoff contributed to the peak in July, and subsurface runoff contributed to the peak in September (Figure 3b). However, CSSP missed the peak during July as most precipitation during the start of wet season (May–June) infiltrated into the soil and increased subsurface runoff (Figure 3a). For the ZMD station, surface runoff is found to be dominant in CSSPv2 (Figure 3d), while subsurface runoff is dominant in CSSP (Figure 3c). Due to the lag time between precipitation and water table increase, runoff in CSSP reaches its peaks 2 months later than the observation (Figures 3a and 3c). The statistics during calibration and validation periods are given in Table 1. As compared with CSSP simulations, CSSPv2 simulations increased correlations by 11–50% and increased NSE by 62–130%.

Given that snowmelt runoff is an important hydrological process in many mountainous regions, we validated the simulation of snow depths by comparing with station observations. The snow model of CSSP and CSSPv2 is the same as that used in the Common Land Model (Dai et al., 2003), where the snowpack can have up to five snow layers depending on the energy and water conditions. As compared with 34 CMA station observations, the CSSPv2 model simulated the snow depths over the Sanjiangyuan region quite well (Figure 4), with the correlation for December–January–February mean snow depth reaching 0.81 during 1980–2008 (Figure 4a). The performance of CSSP is similar to the CSSPv2 because they share the same snow module (not shown). On average, CSSPv2 increased correlation from ERA-Interim by 131% and decreased root-mean-square error (RMSE) by 31% (Figures 4b–4e). However, the snowmelt is not a significant contribution to the streamflow due to a monsoonal climate (Cuo et al., 2014) where the rainy season and peak flows are in the summer (Figure 3).

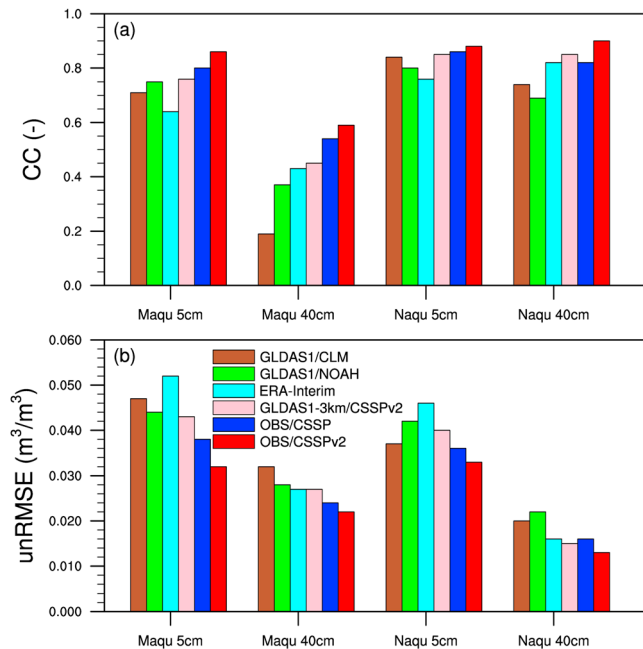


Figure 6. Correlation (CC) and unbiased root-mean-squared error (unRMSE; m^3/m^3) for model simulated daily soil moisture averaged over Maqu and Naqu regions at depths of 5 and 40 cm during May–September. Here GLDAS1-3 km/CSSPv2 represents the CSSPv2 simulations with GLDAS1 meteorological forcings interpolated into 3 km. CSSPv2 = Conjunctive Surface-Subsurface Process version 2; GLDAS = Global Land Data Assimilation System; CSSP = Conjunctive Surface-Subsurface Process; CLM = Community Land Model.

Naqu. Compared with CSSP, CSSPv2 decreased unRMSE for soil moisture by up to 31% and increased correlation by up to 17%.

During summer, GLDAS1/Noah and GLDAS1/Community Land Model (CLM) underestimated soil moisture, which is consistent with previous study (Bi et al., 2016), while ERA-Interim overestimated soil moisture especially at deeper depth (Figure 5). Correlations for two GLDAS1 products range from 0.19 to 0.71 and 0.74 to 0.84 at Maqu and Naqu networks, respectively, while the unRMSE ranges from 0.03 to 0.05 m^3/m^3 and 0.02 to 0.05 m^3/m^3 . Generally, GLDAS1/Noah showed a better performance than GLDAS1/CLM. For the ERA-Interim product, correlation ranges from 0.37 to 0.75 and 0.69 to 0.81 at Maqu and Naqu networks, while unRMSE ranges from 0.03 to 0.05 m^3/m^3 and 0.02 to 0.05 m^3/m^3 . Compared with three reanalysis products, CSSPv2 increased correlation by up to 206% and 30% at Maqu and Naqu networks and decreased unRMSE by up to 38% and 42%.

The CSSPv2 improvements are not only based on model updates but also due to the use of high-resolution forcings. To specify the relative role of model and forcing improvements, we carried out a CSSPv2 simulation with GLDAS1 meteorological forcings interpolated from 1° to 3 km. Figure 6 shows that CSSPv2 simulation with coarse forcing information (pink bars) has similar performance to the GLDAS1 products (brown and green bars) for the soil moisture at depth of 5 cm, suggesting the dominant control of meteorological forcings on surface moisture dynamics. However, the former has a better performance than the latter for the soil moisture simulation at depth of 40 cm, where the correlation increased by 22–137% over Maqu region and by 15–23% over Naqu region, and the unRMSE decreased by up to 16% and 32% over these two regions (Figure 6). The comparison between CSSPv2 simulations driven by GLDAS1 and high-resolution forcings (red bars) shows the importance of meteorological forcings in soil moisture simulation (Figure 6). This is also consistent with our previous study, where gradual improvements were found by incorporating high-resolution meteorological and surface data information (Ji et al., 2017). In short, high-resolution forcing data are critical for a successful high-resolution land surface modeling.

The NSE values range from 0.70 to 0.89 at Yellow River stations, which are better than previous works where NSE values range from 0.49 to 0.85 based on GLDAS1/Variable Infiltration Capacity simulations (Cuo et al., 2013) and 0.31 to 0.89 based on GLDAS1/Noah simulations (Zheng et al., 2017). Bai et al. (2016) also evaluated streamflow simulations of GLDAS1 over the TP, and their results showed that Kling-Gupta efficiency values vary from -0.75 to 0.09 at the TNH and ZMD stations, which are much lower than those from CSSPv2 simulations (Table 1). In short, the CSSPv2 model reasonably simulated monthly streamflow over the Sanjiangyuan region and outperformed many other land surface hydrological models in the literature.

3.2. Soil Moisture

Figure 5 shows the evaluation results for daily soil moisture averaged over the Maqu and Naqu networks. With improved meteorological forcings, both the CSSP and CSSPv2 models simulated the variations of soil moisture quite well. The freeze-thaw cycle was also captured owing to the implementation of the supercooled soil water parameterization proposed by Niu and Yang (2006). As compared with CSSP, CSSPv2 simulated larger soil moisture especially at surface layer (Figures 5a and 5c), which is because of the incorporation of soil organic matter that increased soil porosity. The modified soil thermal parameterization with smaller soil thermal conductivity postponed freezing and thawing times at 40-cm depth, resulted in more liquid soil water during autumn and less during spring (Figures 5b and 5d). The correlations and unbiased root-mean-square error (unRMSE, i.e., the RMSE after removing systematic bias) were calculated during May to September when the soil is not frozen. The unRMSE for CSSPv2 ranges from 0.02 to 0.04 m^3/m^3 at two networks. The correlation for CSSPv2 ranges from 0.59 to 0.86 at Maqu and from 0.87 to 0.90 at

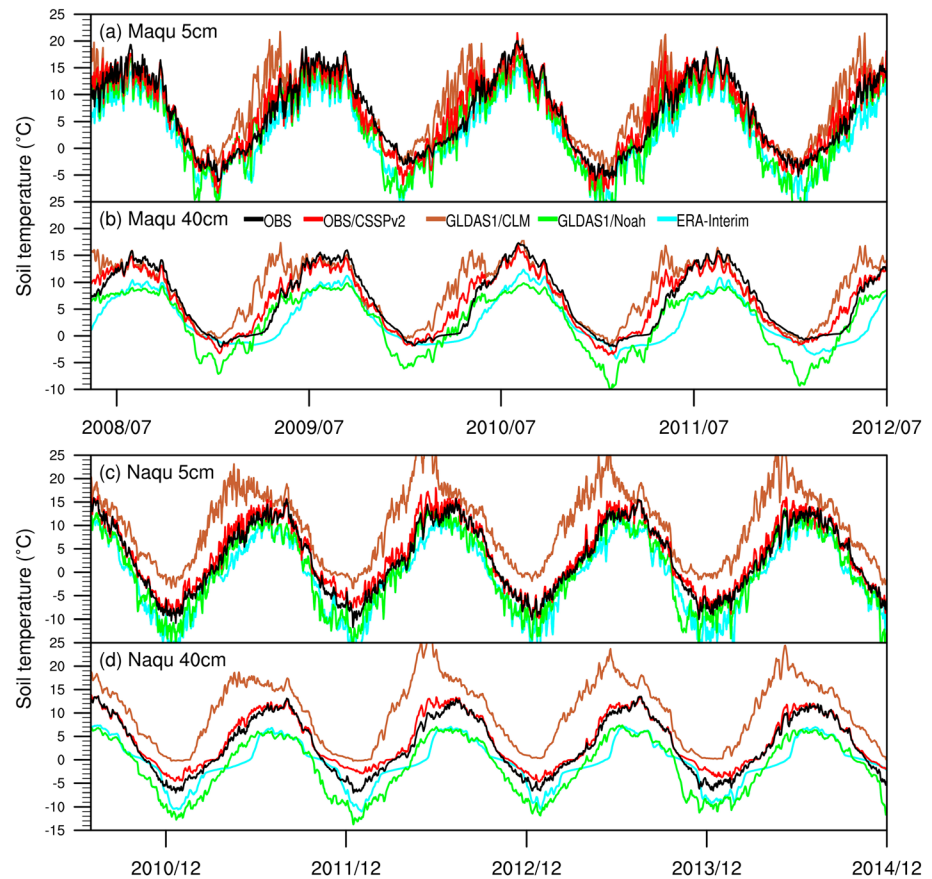


Figure 7. The same as Figure 5 but for daily soil temperature ($^{\circ}\text{C}$) averaged over Maqu and Naqu regions at depths of 5 and 40 cm. The results from CSSP were not shown here due to negligible difference from CSSPv2. CSSPv2 = Conjunctive Surface-Subsurface Process version 2; CSSP = Conjunctive Surface-Subsurface Process. GLDAS = Global Land Data Assimilation System; CLM = Community Land Model.

3.3. Soil Temperature

Figure 7 shows the evaluation results for daily soil temperature, where CSSPv2 captured variations of soil temperature quite well with correlation ranging from 0.95 to 0.99 and unRMSE ranging from 0.94 to 1.96 $^{\circ}\text{C}$ over two networks. The results for CSSP are similar to CSSPv2 (not shown). For the reanalysis, GLDAS1/CLM overestimated soil temperature with correlation and unRMSE being 0.80–0.89 and 3.1–3.8 $^{\circ}\text{C}$, respectively, while GLDAS1/Noah and ERA-Interim underestimated soil temperature especially at deeper depths (Figure 7). Except for low correlation from GLDAS1/CLM, CSSPv2 and the reanalysis simulated soil temperature reasonably in terms of variations. However, CSSPv2 decreased unRMSE by 22–69%, indicating the advantages of high-resolution modeling due to finer surface and forcing data sets.

Besides daily records from Maqu and Naqu networks, annual cycle of monthly soil temperature from eight CMA stations (Figure 1) at five depths was also used for the evaluation. Figures 8a and 8b show that CSSPv2 outperformed three reanalysis data sets significantly, except for lower values than observation during summer. Considering that CMA stations were set up at bare soils while CSSPv2 considered both bare soil and vegetation, the cold bias in summer may be caused by land covers. Similar to the evaluations over the Maqu and Naqu networks, GLDAS1/CLM had a warm bias, while GLDAS1/Noah and ERA-Interim underestimated soil temperature. The probability density functions of bias and unRMSE shown in Figure 8c were derived from kernel density estimation using data from all stations and all depths. Both warm and cold biases occurred in CSSPv2 simulations, with more stations showing cold bias. The biases for the three reanalysis data are much larger than the CSSPv2 (Figure 8c). The unRMSE values for CSSPv2 are less than 2 $^{\circ}\text{C}$, while larger than 2–4 $^{\circ}\text{C}$ for the reanalysis. Mean values of unRMSE are 0.6, 1.0, 1.9, and 1.0 $^{\circ}\text{C}$ for CSSPv2, GLDAS1/Noah, GLDAS1/CLM,

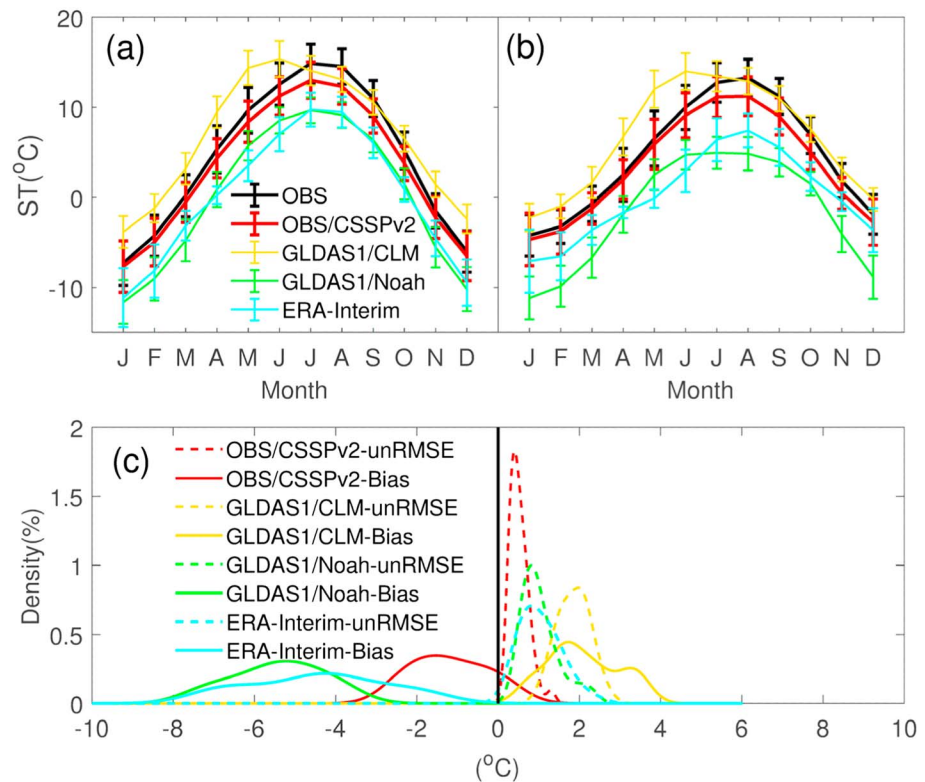


Figure 8. Observed and simulated annual cycles of monthly soil temperature at eight CMA stations at depths of 5 and 40 cm (a and b), and probability distribution functions of bias and unbiased root-mean-square error (unRMSE) for CSSPv2 simulations and three reanalysis data sets validated at depths of 5, 10, 15, 20, and 40 cm (c). Short bars in Figures 8a and 8b represent one standard deviation, solid and dashed lines in Figure 8c represent bias and unRMSE, respectively. The results from CSSP were not shown here due to negligible difference from CSSPv2. CSSPv2 = Conjunctive Surface-Subsurface Process version 2; CSSP = Conjunctive Surface-Subsurface Process; CMA = China Meteorological Administration; GLDAS = Global Land Data Assimilation System; CLM = Community Land Model.

and ERA-Interim, respectively. Therefore, CSSPv2 consistently outperformed the reanalysis products for soil temperature simulations based on three independent sources of observations.

3.4. Evapotranspiration

Figure 9 shows spatial distributions of correlation and RMSE between satellite retrieval (average of the MTE_ET and GLEAM_ET products, see section 2.3 for details) and simulations from CSSPv2 and reanalysis products for ET accumulated during growing seasons (May–September) of 1982–2011. CSSPv2 simulation shows significant correlations (>0.36) over most areas in the Sanjiangyuan region, with higher correlation occurring over Yangtze River and Lancang-Mekong River basins than the Yellow River basin (Figure 9a). The RMSE for ET mostly ranges from 10 to 40 mm (Figure 9b). Correlation and RMSE averaged over the study domain are 0.83 and 9 mm, respectively, for the CSSPv2 ET simulation. The results for previous CSSP model are similar, but the RMSE increased by 33% as compared with CSSPv2 (Figures 9c and 9d).

Two GLDAS1 products show significant correlations over upper reaches of the Sanjiangyuan region (Figures 9e and 9g), while ERA-Interim has a high correlation over the eastern parts (Figure 9i). RMSE values for two GLDAS1 data sets are larger than 40 mm over most regions, where the GLDAS1/Noah has larger RMSE than the GLDAS1/CLM in the eastern part (Figures 9f and 9h). ERA-Interim has the largest RMSE over the western part, which is greater than 120 mm (Figure 9j). On average, correlations are 0.57, 0.7, and -0.16 , and RMSE values are 50, 42, and 115 mm for GLDAS1/CLM, GLDAS1/Noah, and ERA-Interim respectively. Compared with three reanalysis data sets, CSSPv2 increased correlation by 18–46% and decreased RMSE by 79–92% for the ET simulations over the Sanjiangyuan region during the growing seasons.

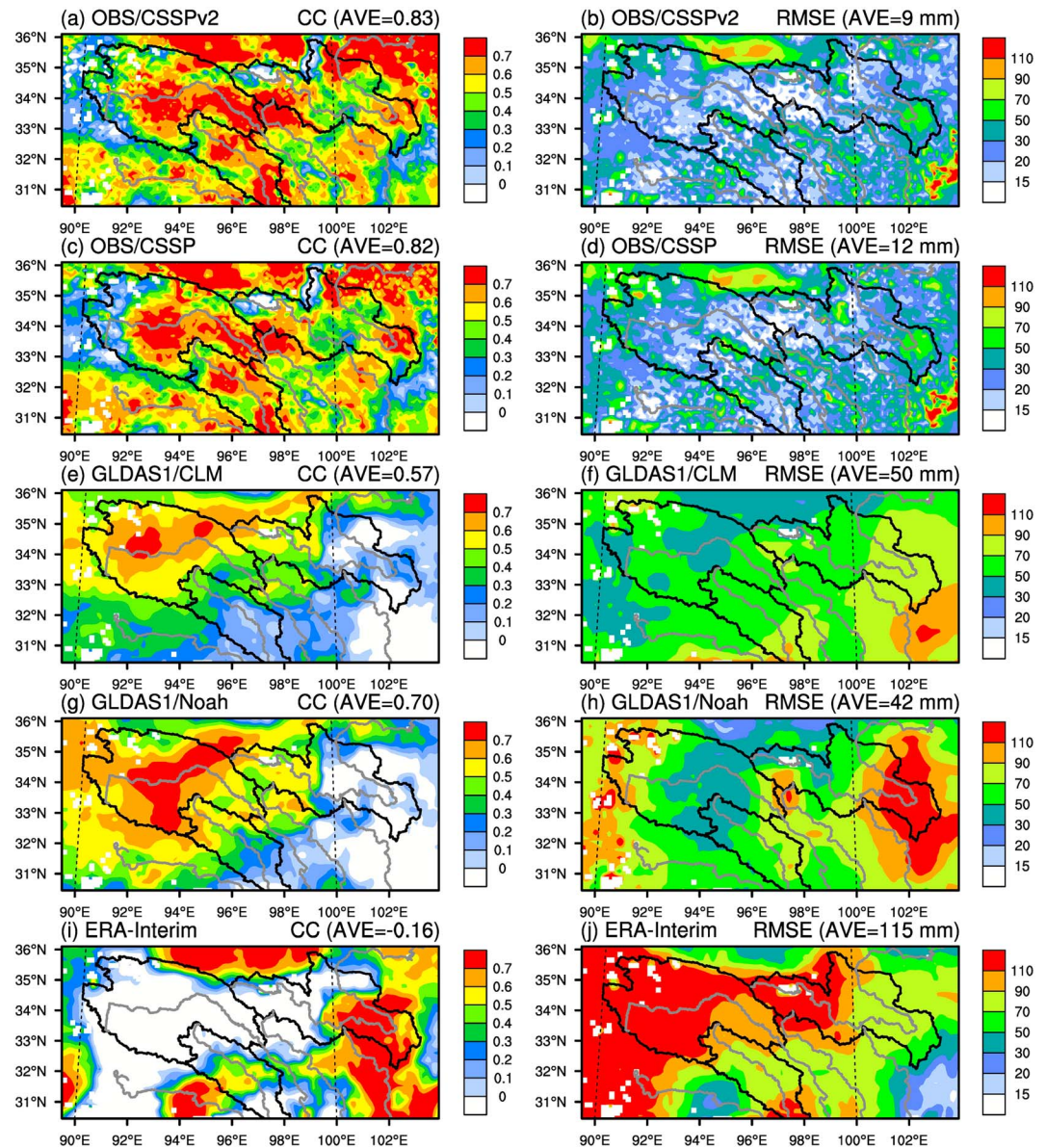


Figure 9. Evaluation of ET simulations over the Sanjiangyuan region. Spatial distributions of correlation coefficient (CC) and RMSE between satellite retrievals (ensemble mean of the MTE_ET and GLEAM_ET products) and simulations from CSSPv2 and three reanalysis products for ET accumulated during the growing seasons (May–September) of 1982–2011. For each grid point, CC and RMSE were calculated based on the time series of May–September mean ET during 1982–2011, and the numbers in the brackets in the upper-right corner of each panel are the CC and RMSE for the time series for regional mean ET averaged during May–September. CSSPv2 = Conjunctive Surface-Subsurface Process version 2; CSSP = Conjunctive Surface-Subsurface Process; GLDAS = Global Land Data Assimilation System; CLM = Community Land Model; RMSE = root-mean-square error; MTE_ET = Model Tree Ensemble evapotranspiration; GLEAM_ET = Global Land Evaporation Amsterdam Model evapotranspiration; ET = evapotranspiration.

3.5. Terrestrial Water Storage Change

Figure 10 shows the correlation and RMSE for monthly TWSC during 2003–2014, as verified against GRACE TWSC. CSSPv2 simulation shows significant correlations ($CC > 0.6$) over the Sanjiangyuan region, except for the lower reaches of headwaters of the Yellow River and Lancang-Mekong River (Figure 10a). CSSP simulation has a little lower correlation than CSSPv2 (Figure 10c). Two GLDAS1 products, however, have low correlations over most areas (Figures 10e and 10g). The ERA-Interim has higher correlation over eastern part

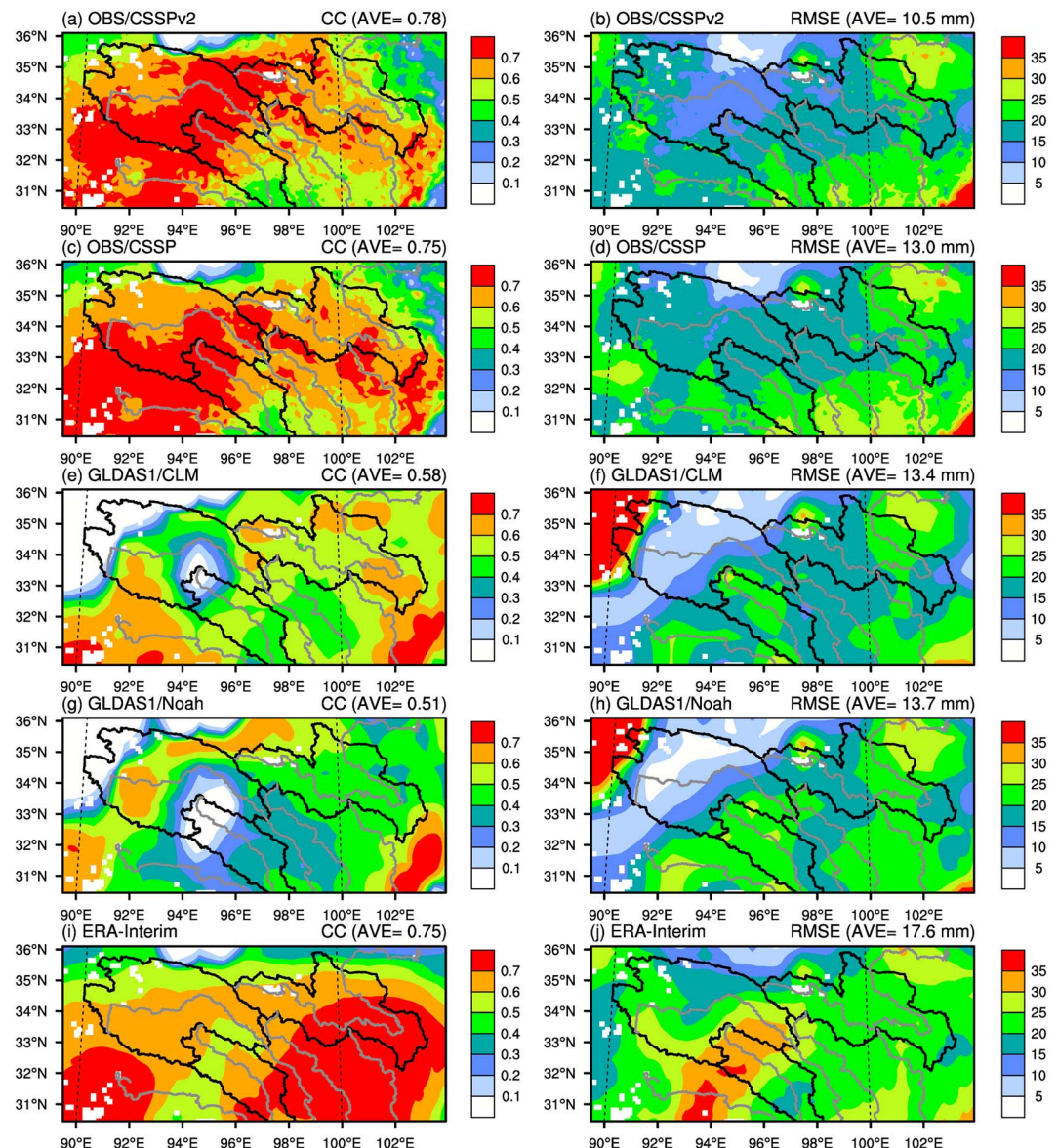


Figure 10. The same as Figure 9 but for monthly terrestrial water storage change (TWSC) during 2003–2014. For each grid point, CC and RMSE were calculated based on the time series of monthly TWSC during 2003–2014, and the numbers in the brackets in the upper-right corner of each panel are the CC and RMSE for the time series for regional mean monthly TWSC. Here the reference is ensemble mean of three GRACE satellite data sets. CSSPv2 = Conjunctive Surface-Subsurface Process version 2; CSSP = Conjunctive Surface-Subsurface Process; GLDAS = Global Land Data Assimilation System; RMSE = root-mean-square error.

(Figure 10i), which is consistent with ET results (Figure 9g). ERA-Interim has the largest errors, while CSSPv2 has the least (Figures 10b, 10d, 10f, 10h, and 10j). Correlation and RMSE for regional mean monthly TWSC between CSSPv2 simulations and GRACE observations are 0.78 and 10.5 mm, respectively. Compared with CSSP, CSSPv2 reduced RMSE by 24%. Compared with two GLDAS1 products, CSSPv2 increased correlation by 34–53% and reduced RMSE by 23%. Compared with the ERA-Interim, although CSSPv2 only increased correlation by 4%, it reduced RMSE by 40% due to better representation of the actual magnitude of TWSC.

4. Simulation of Hydrological Changes Over the Sanjiangyuan Region

After evaluating the CSSPv2 model at daily to seasonal time scales, this section will assess whether the model can reproduce the long-term trends for hydrological variables over the Sanjiangyuan region.

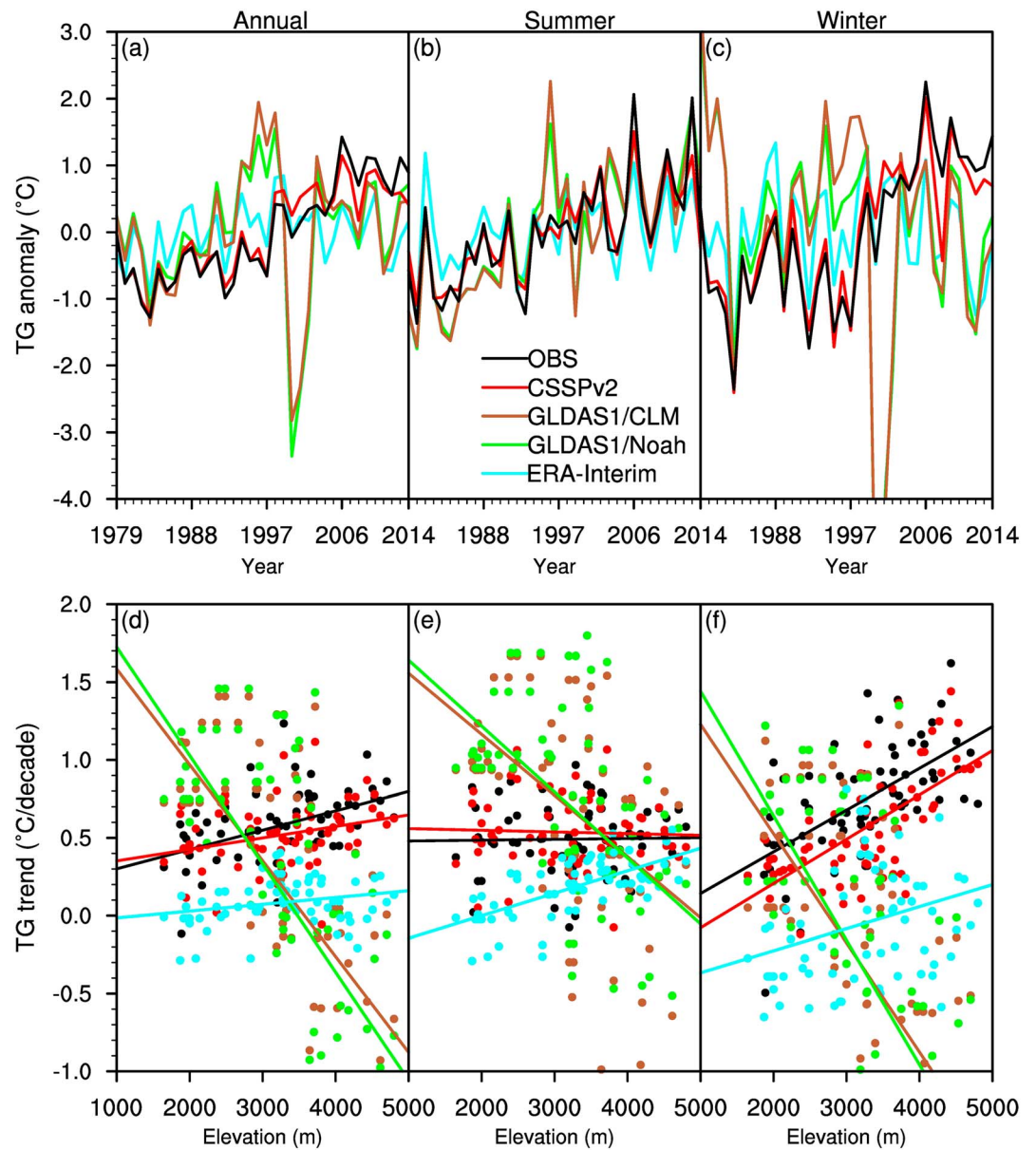


Figure 11. Observed and simulated annual (a), summer (b), and winter (c) mean ground temperature (TG) anomalies averaged over 73 CMA stations during 1979–2014, and scatterplots of stations' elevations and their corresponding annual (d), summer (e), and winter (f) TG trends. Solid lines in Figures 11d–11f are linear regressions between elevation and TG trends. CSSPv2 = Conjunctive Surface-Subsurface Process version 2; GLDAS = Global Land Data Assimilation System; CLM = Community Land Model; CMA = China Meteorological Administration.

4.1. Ground Temperature Change

Figure 11a shows time series of annual TG anomalies averaged over 73 CMA stations (Figure 1). CSSPv2 simulated a $0.51\text{ }^{\circ}\text{C}/\text{decade}$ warming rate, which is smaller than the observation ($0.61\text{ }^{\circ}\text{C}/\text{decade}$). Three reanalysis data sets showed the same trends as observation before 1997, but they failed to capture the warming trends afterward (Figure 11a). As a result, their warming trends are less than $0.25\text{ }^{\circ}\text{C}/\text{decade}$ during 1979–2014, which are less than 41% of the observed trend. The unrealistic drop in TG around 2000 for the GLDAS1 models might be related to the uncertainty in the meteorological forcing data, where different sources of forcings were used (Figure 11a). To diagnose the failure after 1998 for the reanalysis products, summer and winter TG anomalies are shown in Figures 11b and 11c. It is obvious that all simulations show increasing trends during

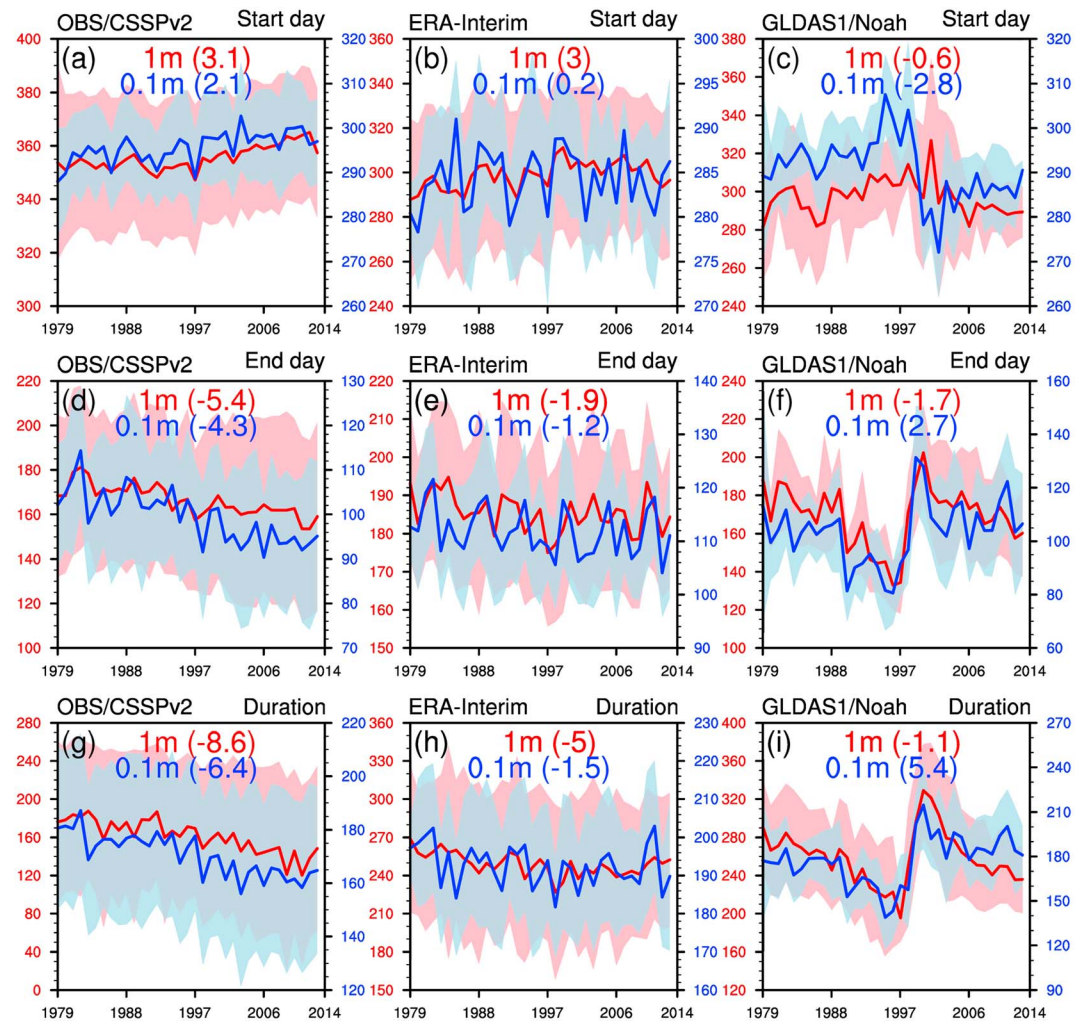


Figure 12. Time series of start and end frozen dates, as well as frozen durations averaged over the Sanjiangyuan region for CSSPv2, ERA-Interim, and Noah simulations. If the soil temperature are below (above) 0 for five consecutive days, the first day within the 5 days was regarded as the start (end) frozen date. Red and blue lines represent regional mean values at depths of 1 and 0.1 m, respectively, with one standard deviations shown by pink and light blue shades. The numbers in brackets are linear trends (day/decade). CSSPv2 = Conjunctive Surface-Subsurface Process version 2; GLDAS = Global Land Data Assimilation System.

summer. Specifically, CSSPv2 produced a warming rate of 0.44 °C/decade, which is close to the observation (0.48 °C/decade), while two GLDAS1 products overestimated the rate by 46% and ERA-Interim underestimated by 56% (Figure 11b). During winter, only CSSPv2 shows a 0.6 °C/decade warming trend, which is consistent with the observed 0.75 °C/decade, while three reanalysis data sets show decreasing trends (Figure 11c). Figures 11b and 11c also suggest that the uncertainty in GLDAS1 forcings around 2000 mainly exists in cold seasons. This suggests that the Sanjiangyuan region has a faster warming in winter than summer, which was simulated well by the CSSPv2 model, but global reanalysis products failed to capture the cold season warming trend.

In addition to the average results among stations, trends for annual, summer, and winter TG for each station were plotted against their elevations (Figures 11d–11f). For the annual and winter mean TG, there is obvious elevation-dependent warming (Pepin et al., 2015) over the Sanjiangyuan region, which was simulated by the CSSPv2 model quite well. However, GLDAS1 failed to capture the relationship, and ERA-Interim presented a much weaker positive correlation (Figures 11d and 11f). For the summer time, there is no significant correlation between elevations and TG trends, but GLDAS1 produced a negative relation (Figure 11e).

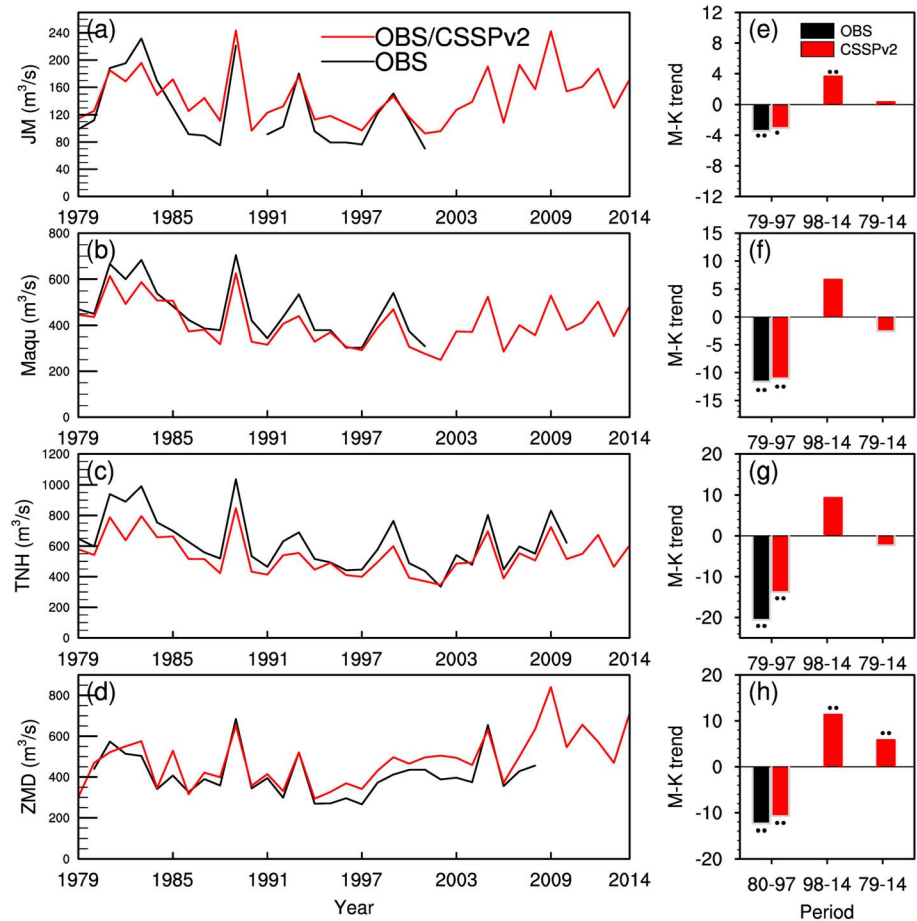


Figure 13. Observed and CSSPv2 simulated annual streamflow (m^3/s) at four hydrological stations (a–d) and their Mann-Kendall trends ($\text{m}^3/\text{s}/\text{year}$) during different periods. One dot and two dots are the significances of the trends at the 90% and 95% confidence levels, respectively. CSSPv2 = Conjunctive Surface-Subsurface Process version 2.

4.2. Frozen Soil Change

The warming temperature resulted in significant changes in frozen soils over the Sanjiangyuan region. Figure 12 shows the start (top rows) and end (middle rows) days for the frozen soil at depths of 10 cm and 1 m, and their frozen durations (bottom rows). The results for GLDAS1/CLM were not shown because there are hardly any frozen soils in the simulation due to the warm bias. First, both CSSPv2 and ERA-Interim show decreasing trends for the end frozen date and frozen duration, and increasing trend for the start frozen date (Figures 12a and 12b, 12d and 12e, and 12g and 12h). GLDAS1/Noah shows some differences due to the abrupt changes in 1996 and 2000, which might be partly caused by inhomogeneous forcing data. Second, ERA-Interim has smaller trends compared with CSSPv2. Guo and Wang (2013) did a simulation over the TP during 1981–2010 and found that start frozen date delayed by 3.8–4.0 day/decade, end frozen date advanced by 4.6–5.9 day/decade, and frozen duration reduced by 8.6–9.7 day/decade at 1-m depth. Li et al. (2012) analyzed changes in near surface soil freeze-thaw cycle over TP during 1988–2007 by using remote sensing data and found that start frozen date delayed by 5 day/decade, end frozen date advanced by 7 day/decade, and frozen duration shorten by 16.8 day/decade. Generally, CSSPv2 simulations are more consistent with previous works than the reanalysis data.

4.3. Streamflow Change

Figure 13 shows that streamflow decreased first and then started to recover over the headwaters of the Yellow River and Yangtze River basins during 1979–2014, but the recovery time for the Yangtze River was earlier than that for the Yellow River (Figures 13a–13d). During 1979–1997, streamflow at JM, Maqu, TNH, and

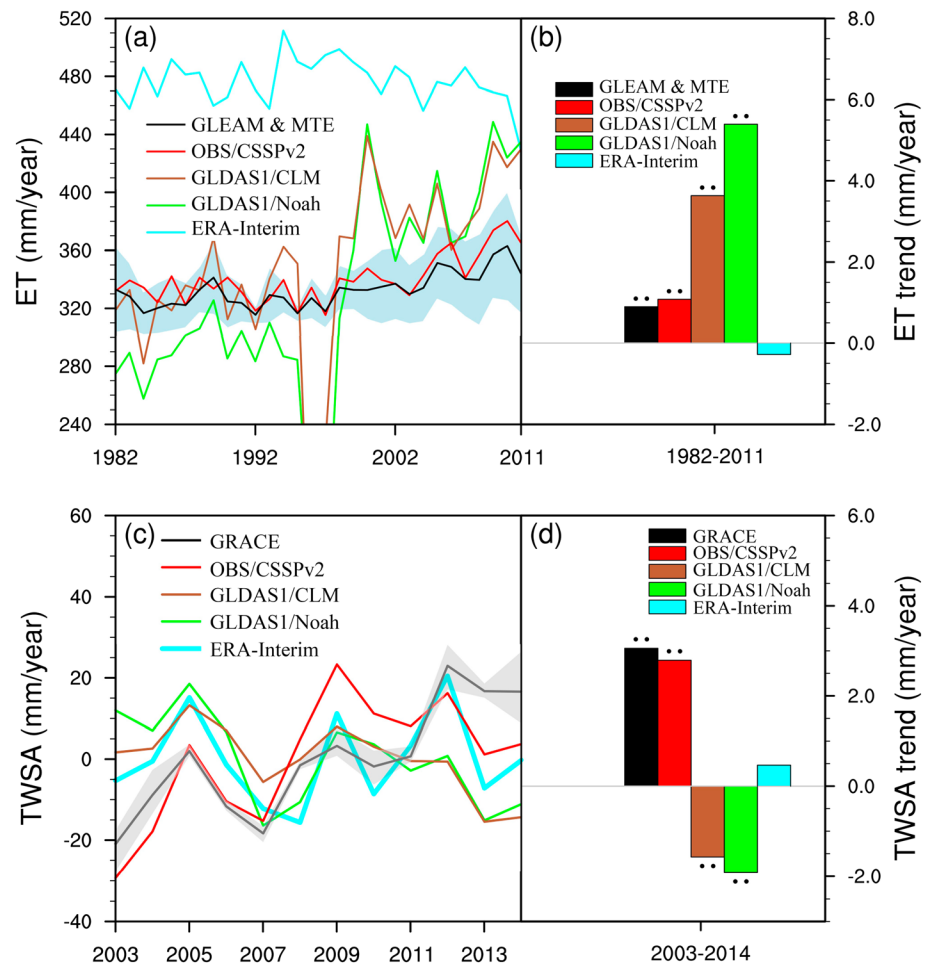


Figure 14. (a) Observed and simulated annual evapotranspiration (ET) averaged over the Sanjiangyuan region during 1982–2011 and (b) the corresponding M-K trends. (c and d) The same as Figures 14a and 14b but for annual terrestrial water storage anomaly (TWSA) during 2003–2014. GLEAM = Global Land Evaporation Amsterdam Model; MTE = Model Tree Ensemble; CSSPv2 = Conjunctive Surface-Subsurface Process version 2; CLM = Community Land Model; GLDAS = Global Land Data Assimilation System; GRACE = Gravity Recovery and Climate Experiment.

ZMD stations decreased significantly ($p < 0.05$) at rates of -3.4 , -11.6 , -20.6 , and -12.4 $\text{m}^3/\text{s}/\text{year}$, respectively. CSSPv2 simulations captured 67–95% of the trends with rates of -3.1 , -11.0 , -13.8 , and -10.7 $\text{m}^3/\text{s}/\text{year}$ (Figures 13e–13h). During 1998–2014, CSSPv2 simulations show significant increases at JM and ZMD stations while insignificant increases at Maqu and TNH stations. For the whole period (1979–2014), Yellow River headwater stations do not show significant changes while Yangtze River headwater station (ZMD) show significant increase in streamflow ($p < 0.05$).

4.4. ET and TWS Changes

Figures 14a–14b show that CSSPv2 reasonably captured the significant increasing trend ($p < 0.05$) in annual ET averaged over the Sanjiangyuan region during 1997–2011. Similar to the frozen soil, two GLDAS1 products had an abrupt change around 1997 due to forcing data inconsistency (Figure 14a), which resulted in overestimated upward trends in ET (Figure 14b). The ERA-Interim generally overestimated the magnitude of ET (Figure 14a) and showed an insignificant decreasing trend (Figure 14b).

Figures 14c and 14d show that GRACE-measured annual terrestrial water storage anomaly (TWSA) averaged over the Sanjiangyuan region increased significantly during 2003–2014 ($p < 0.05$). CSSPv2 captured 93% of the increasing trend, while ERA-Interim only captured 17% (Figure 14d). Two GLDAS1 products, however, produced significant decreasing trends in TWSA (Figure 14d), which is associated with the overestimated increasing trends in ET (Figure 14b).

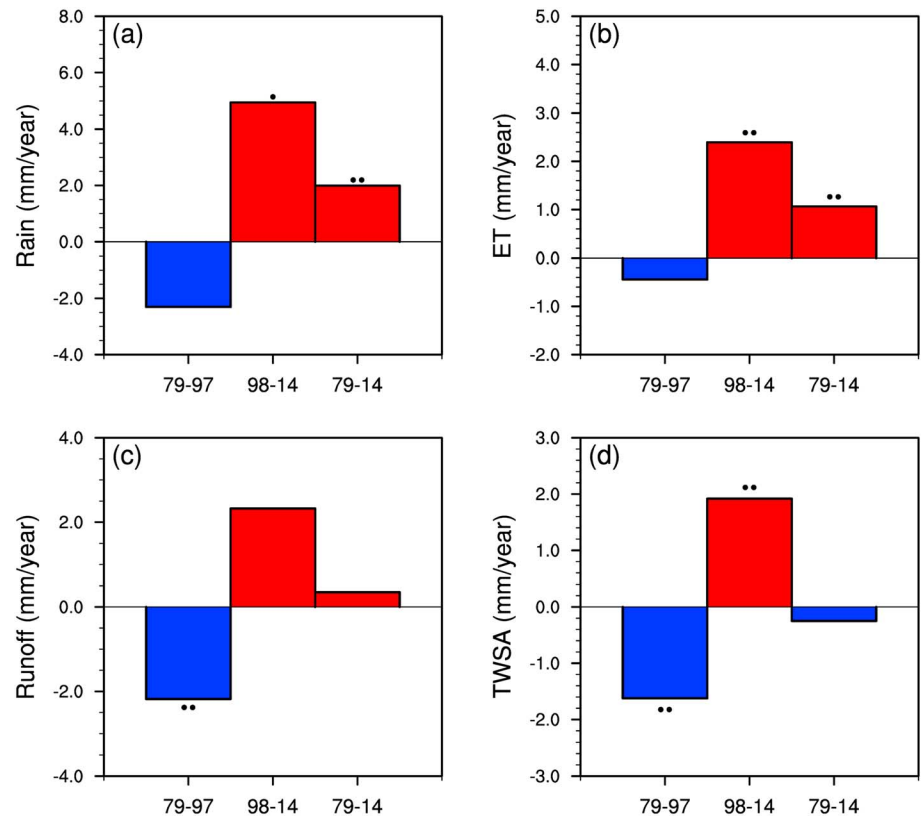


Figure 15. Mann-Kendall trends for different hydrological variables during different periods based on CSSPv2 simulation, with one and two dots showing the significance of the trends at the 90% and 95% confidence levels. CSSPv2 = Conjunctive Surface-Subsurface Process version 2; TWSA = terrestrial water storage anomaly; ET = evapotranspiration.

4.5. Hydrological Changes Over the Sanjiangyuan Region During 1979–2014

After the comprehensive evaluations above, we believe the CSSPv2 model simulated the hydrological cycle over the Sanjiangyuan region reasonably. Therefore, we conclude by showing trends of regional mean hydrological variables in Figure 15. During 1979–1997, all the land surface hydrological variables showed decreasing trends, with significant trends occurred in runoff and TWSA ($p < 0.05$). During 1998–2014, increased precipitation ($p < 0.1$) and temperature led to significant increase in ET ($p < 0.05$). However, the rate for increasing ET is slower than increasing precipitation (Figures 15a and 15b), resulted in increases in runoff ($p > 0.1$) and TWSA ($p < 0.05$) during 1998–2014. For the entire period (1979–2014), the warming and wetting trends ($p < 0.05$) over the Sanjiangyuan region led to increased ET ($p < 0.05$) and insignificant changes in runoff and TWSA.

5. Conclusions and Discussion

With the influence of climate and land cover change, terrestrial hydrological cycle over the Sanjiangyuan region in eastern TP experienced significant changes. However, a reliable and systematic analysis on the changes in different components in the hydrological cycle (e.g., streamflow, soil moisture and temperature, ET, total water storage) is absent due to sparse observations and large uncertainty in the models and reanalysis data. As the first part of a series toward providing a reliable high-resolution land surface modeling and attribution of hydrological changes over the Sanjiangyuan region during the past few decades, this paper introduced a few updates to the CSSP (Liang et al., 2012; Yuan & Liang, 2011) model including the storage-based runoff generation scheme, soil organic matter, and thermal parameterizations, which was named as CSSPv2. High-resolution (3 km) land surface simulations were carried out over the Sanjiangyuan region during 1979–2014 and were then systematically evaluated against multisource observations including in situ measurements and satellite retrievals. They were also compared with GLDAS1 and ERA-Interim reanalysis products.

Compared with CSSP, CSSPv2 increased NSE by 62–130% and reduced relative RMSE by 34–51% in streamflow simulation, increased correlation by up to 17%, and decreased unbiased RMSE by up to 31% for soil moisture modeling after considering the soil organic matter. Compared with reanalysis products, CSSPv2 improved correlation by up to 206%, 46%, and 53% for soil moisture, ET, and monthly TWSC, respectively, and reduced RMSE by up to 30%, 69%, 92%, and 40% for soil moisture, soil temperature, ET, and monthly TWSC, respectively. CSSPv2 well captured the elevation-dependent TG warming trends, ERA-Interim underestimated them, and GLDAS1.0 products showed negative relation. CSSPv2 well simulated decreased frozen durations with delayed freeze and earlier melt, which were consistent with previous studies. There is a significant increasing trend ($p < 0.05$) in satellite-retrieved ET averaged over the Sanjiangyuan region during 1982–2011, which was captured well by CSSPv2. However, ERA-Interim showed no significant trend and GLDAS1 products overestimated the trend greatly. GRACE TWSA showed a significant increasing trend ($p < 0.05$) during 2003–2014, which was successfully simulated by the CSSPv2, while ERA-Interim showed no significant trend and GLDAS1 products even showed a falsely decreasing trend.

Although the performance of CSSPv2 is satisfactory, some issues need to be solved in the future. First, considering the soil organic matter increases soil moisture over the top layers, but there are underestimations during summer seasons especially at Maqu network that may be caused by other hydrological processes such as hydraulic conductivity parameterizations (Zheng et al., 2015). Second, the effect of lateral flow processes on the high-resolution simulation over the Sanjiangyuan region is not clear. Ji et al. (2017) performed a hyperresolution simulation over western United States mountainous areas and found that the lateral subsurface flow affected the simulations of soil moisture and latent heat significantly at 100-m resolution. Similar studies could be carried out over the Sanjiangyuan region if the quality of meteorological forcings and surface data sets can be improved for such hyperresolution modeling. Third, the influences of anthropogenic and natural climate change, as well as land cover change on the land surface hydrological changes over the Sanjiangyuan headwater region, are still unknown, and they will be analyzed in the second part of the series (Ji & Yuan, 2018).

Acknowledgments

We thank three anonymous reviewers and the Editor Paul Dirmeyer for their helpful comments. This work was supported by National Natural Science Foundation of China (91547103), National Key R&D Program of China (2018YFA0606002), and the Startup Foundation for Introducing Talent of NUIST. The meteorological forcing and the Naqu soil moisture and temperature observation data sets were provided by Data Assimilation and Modeling Center for Tibetan Multispheres at Chinese Academy of Sciences. We thank the GIMMS group, GLEAM group, and Jung for providing the NDVI and reference ET data. GRACE data are available at <http://grace.jpl.nasa.gov>, supported by the NASA MEaSUREs Program.

References

- Bai, P., Liu, X., Yang, T., Liang, K., & Liu, C. (2016). Evaluation of streamflow simulation results of land surface models in GLDAS on the Tibetan plateau. *Journal of Geophysical Research: Atmospheres*, 121, 12,180–12,197. <https://doi.org/10.1002/2016JD025501>
- Baldocchi, D., Falge, E., Gu, L., Olson, R., Hollinger, D., Running, S., & Wofsy, S. (2001). FLUXNET: A new tool to study the temporal and spatial variability of ecosystem-scale carbon dioxide, water vapor, and energy flux densities. *Bulletin of the American Meteorological Society*, 82(11), 2415–2434. [https://doi.org/10.1175/1520-0477\(2001\)082%3C2415:FANTTS%3E2.3.CO;2](https://doi.org/10.1175/1520-0477(2001)082%3C2415:FANTTS%3E2.3.CO;2)
- Bi, H., Ma, J., Zheng, W., & Zeng, J. (2016). Comparison of soil moisture in GLDAS model simulations and in situ observations over the Tibetan plateau. *Journal of Geophysical Research: Atmospheres*, 121, 2658–2678. <https://doi.org/10.1002/2015JD024131>
- Bierkens, M. F. P., Bell, V. A., Burek, P., Chaney, N., Condon, L. E., David, C. H., et al. (2015). Hyper-resolution global hydrological modelling: What is next? "Everywhere and locally relevant". *Hydrological Processes*, 29(2), 310–320. <https://doi.org/10.1002/hyp.10391>
- Chen, Y. Y., Yang, K., Qin, J., Zhao, L., Tang, W., & Han, M. (2013). Evaluation of AMSR-E retrievals and GLDAS simulations against observations of a soil moisture network on the central Tibetan plateau. *Journal of Geophysical Research: Atmospheres*, 118, 4466–4475. <https://doi.org/10.1002/jgrd.50301>
- Chen, Y. Y., Yang, K., Tang, W. J., Qin, J., & Zhao, L. (2012). Parameterizing soil organic carbon's impacts on soil porosity and thermal parameters for eastern Tibet grasslands. *Science China Earth Sciences*, 55(6), 1001–1011. <https://doi.org/10.1007/s11430-012-4433-0>
- Choi, H. I. (2006). 3-D volume averaged soil-moisture transport model: A scalable scheme for representing subgrid topographic control in land-atmosphere interactions, University of Illinois at Urbana, Champaign, 93-95pp.
- Choi, H. I., Kumar, P., & Liang, X. Z. (2007). Three-dimensional volume-averaged soil moisture transport model with a scalable parameterization of subgrid topographic variability. *Water Resources Research*, 43, W04414. <https://doi.org/10.1029/2006WR005134>
- Choi, H. I., & Liang, X. Z. (2010). Improved terrestrial hydrologic representation in mesoscale land surface models. *Journal of Hydrometeorology*, 11(3), 797–809. <https://doi.org/10.1175/2010JHM1221.1>
- Choi, H. I., Liang, X. Z., & Kumar, P. (2013). A conjunctive surface–subsurface flow representation for mesoscale land surface models. *Journal of Hydrometeorology*, 14(5), 1421–1442. <https://doi.org/10.1175/JHM-D-12-0168.1>
- Cuo, L., Zhang, Y., Gao, Y., Hao, Z., & Cairang, L. (2013). The impacts of climate change and land cover/use transition on the hydrology in the upper Yellow River basin, China. *Journal of Hydrology*, 502(2), 37–52. <https://doi.org/10.1016/j.jhydrol.2013.08.003>
- Cuo, L., Zhang, Y., Zhu, F., & Liang, L. (2014). Characteristics and changes of streamflow on the Tibetan plateau: A review. *Journal of Hydrology: Regional Studies*, 2(C), 49–68. <https://doi.org/10.1016/j.ejrh.2014.08.004>
- Dai, A. (2013). Increasing drought under global warming in observations and models. *Nature Climate Change*, 3(1), 52–58. <https://doi.org/10.1038/NCLIMATE1633>
- Dai, Y., Dickinson, R. E., & Wang, Y. P. (2004). A two-big-leaf model for canopy temperature, photosynthesis, and stomatal conductance. *Journal of Climate*, 17(12), 2281–2299. [https://doi.org/10.1175/1520-0442\(2004\)017<2281:ATMFC2>2.0.CO;2](https://doi.org/10.1175/1520-0442(2004)017<2281:ATMFC2>2.0.CO;2)
- Dai, Y., Zeng, X., Dickinson, R. E., Baker, I., Bonan, G. B., Bosilovich, M. G., et al. (2003). The Common Land Model. *Bulletin of the American Meteorological Society*, 84(8), 1013–1024. <https://doi.org/10.1175/BAMS-84-8-1013>
- Dai, Y. J., Shangquan, W., Duan, Q. Y., Liu, B. Y., Fu, S. H., & Niu, G. Y. (2013). Development of a China dataset of soil hydraulic parameters using pedotransfer functions for land surface modeling. *Journal of Hydrometeorology*, 14(3), 869–887. <https://doi.org/10.1175/Jhm-D-12-0149.1>

- Dee, D. P., Uppala, S., Simmons, A., Berrisford, P., Poli, P., Kobayashi, S., et al. (2011). The ERA-Interim reanalysis: Configuration and performance of the data assimilation system. *Quarterly Journal of the Royal Meteorological Society*, *137*(656), 553–597. <https://doi.org/10.1002/qj.828>
- Dente, L., Vekerdy, Z., Wen, J., & Su, Z. (2012). Maqu network for validation of satellite-derived soil moisture products. *International Journal of Applied Earth Observation and Geoinformation*, *17*, 55–65. <https://doi.org/10.1016/j.jag.2011.11.004>
- Guo, D. L., & Wang, H. J. (2013). Simulation of permafrost and seasonally frozen ground conditions on the Tibetan plateau, 1981–2010. *Journal of Geophysical Research: Atmospheres*, *118*, 5216–5230. <https://doi.org/10.1002/jgrd.50457>
- Gupta, H. V., Kling, H., Yilmaz, K. K., & Martinez, G. F. (2009). Decomposition of the mean squared error and NSE performance criteria: Implications for improving hydrological modelling. *Journal of Hydrology*, *377*(1–2), 80–91. <https://doi.org/10.1016/j.jhydrol.2009.08.003>
- He, J., & Yang, K. (2011). China meteorological forcing dataset. *Cold and Arid Regions Science Data Center, Lanzhou*. <https://doi.org/10.3972/westdc.002.2014.db>
- Intergovernmental Panel on Climate Change (2013). Summary for policymakers. In *Climate change 2013: The physical science basis. Contribution of Working Group I to the Fifth Assessment Report of the Intergovernmental Panel on Climate Change* (27 pp.). Cambridge, UK and New York: Cambridge University Press.
- Ji, P., & Yuan, X. (2018). High resolution land surface modeling of hydrological changes over the Sanjiangyuan region in the eastern Tibetan plateau: 2. Impact of climate and land cover change. *Journal of Advances in Modeling Earth Systems*, *10*. <https://doi.org/10.1029/2018MS001413>
- Ji, P., Yuan, X., & Liang, X.-Z. (2017). Do lateral flows matter for the hyperresolution land surface modeling? *Journal of Geophysical Research: Atmospheres*, *122*, 12,077–12,092. <https://doi.org/10.1002/2017JD027366>
- Jiang, C., & Zhang, L. (2016). Effect of ecological restoration and climate change on ecosystems: A case study in the three-rivers headwater region, China. *Environmental Monitoring and Assessment*, *188*(6), 382. <https://doi.org/10.1007/s10661-016-5368-2>
- Jung, M., Reichstein, M., & Bondeau, A. (2009). Towards global empirical upscaling of FLUXNET eddy covariance observations: Validation of a model tree ensemble approach using a biosphere model. *Biogeosciences*, *6*(10), 2001–2013. <https://doi.org/10.5194/bg-6-2001-2009>
- Jung, M., Reichstein, M., Ciais, P., Seneviratne, S. I., Sheffield, J., Goulden, M. L., et al. (2010). Recent decline in the global land evapotranspiration trend due to limited moisture supply. *Nature*, *467*(7318), 951–954. <https://doi.org/10.1038/nature09396>
- Landerer, F. W., & Swenson, S. C. (2012). Accuracy of scaled GRACE terrestrial water storage estimates. *Water Resources Research*, *48*, W04531. <https://doi.org/10.1029/2011WR011453>
- Li, X., Jin, R., Pan, X., Zhang, T., & Guo, J. (2012). Changes in the near-surface soil freeze–thaw cycle on the Qinghai-Tibetan plateau. *International Journal of Applied Earth Observation and Geoinformation*, *17*(1), 33–42.
- Liang, X., Lettenmaier, D. P., Wood, E. F., & Burges, S. J. (1994). A simple hydrologically based model of land surface water and energy fluxes for general circulation models. *Journal of Geophysical Research*, *99*(D7), 14,415–14,428. <https://doi.org/10.1029/94JD00483>
- Liang, X. Z., Xu, M., Yuan, X., Ling, T., Choi, H. I., Zhang, F., et al. (2012). Regional climate–weather research and forecasting model. *Bulletin of the American Meteorological Society*, *93*(9), 1363–1387. <https://doi.org/10.1175/BAMS-D-11-00180.1>
- Liu, X., Zhang, J., & Zhu, X. (2014). Spatiotemporal changes in vegetation coverage and its driving factors in the Three-River Headwaters Region during 2000–2011. *Journal of Geographical Sciences*, *24*(2), 288–302. <https://doi.org/10.1007/s11442-014-1088-0>
- LP-DACC: NASA land processes distributed active archive center. (2007). MODIS/Terra vegetation indices monthly L3 global 0.05Deg CMG (MOD13C2), Version 005. USGS/Earth Resources Observation and Science (EROS) Center, Sioux Falls.
- Manabe, S. (1969). Climate and the ocean circulation: I. The atmospheric circulation and the hydrology of the Earth's surface. *Monthly Weather Review*, *97*(11), 739–774. [https://doi.org/10.1175/1520-0493\(1969\)097<0739:CATOC>2.3.CO;2](https://doi.org/10.1175/1520-0493(1969)097<0739:CATOC>2.3.CO;2)
- Martens, B., Miralles, D. G., Lievens, H., Schalie, R. V. D., Jeu, R. A. M. D., Fernándezprieto, D., et al. (2017). Gleaf v3: Satellite-based land evaporation and root-zone soil moisture. *Geoscientific Model Development*, *10*(5), 1903–1925. <https://doi.org/10.5194/gmd-10-1903-2017>
- Maxwell, R. M., & Condon, L. E. (2016). Connection between groundwater flow and transpiration partitioning. *Science*, *353*(6297), 377–380. <https://doi.org/10.1126/science.aaf7891>
- Melsen, L. A., Teuling, A. J., Torfs, P. J. J. F., Uijlenhoet, R., Mizukami, N., & Clark, M. P. (2016). Hess opinions: The need for process-based evaluation of large-domain hyper-resolution models. *Hydrology and Earth System Sciences*, *20*(3), 1069–1079. <https://doi.org/10.5194/hess-20-1069-2016>
- Milly, P. C., Wetherald, R. T., Dunne, K. A., & Delworth, T. L. (2002). Increasing risk of great floods in a changing climate. *Nature*, *415*(6871), 514–517. <https://doi.org/10.1038/415514a>
- Miralles, D. G., Holmes, T. R. H., de Jeu, R. A. M., Gash, J. H., Meesters, A. G. C. A., & Dolman, A. J. (2011). Global land-surface evaporation estimated from satellite-based observations. *Hydrology and Earth System Sciences*, *15*(2), 453–469. <https://doi.org/10.5194/hess-15-453-2011>
- Niu, G.-Y., Paniconi, C., Troch, P. A., Scott, R. L., Durcik, M., Zeng, X., et al. (2014). An integrated modelling framework of catchment-scale ecohydrological processes: 1. Model description and tests over an energy-limited watershed. *Ecohydrology*, *7*(2), 427–439. <https://doi.org/10.1002/eco.1362>
- Niu, G. Y., & Yang, Z. L. (2006). Effects of frozen soil on snowmelt runoff and soil water storage at a continental scale. *Journal of Hydrometeorology*, *7*(5), 937–952. <https://doi.org/10.1175/JHM538.1>
- Niu, G. Y., Yang, Z. L., Dickinson, R. E., & Gulden, L. E. (2005). A simple TOPMODEL-based runoff parameterization (SIMTOP) for use in global climate models. *Journal of Geophysical Research*, *110*, D21106. <https://doi.org/10.1029/2005JD006111>
- Oleson, K. W., Lawrence, D. M., Bonan, G. B., Drewniak, B., Huang, M., & Koven, C. D., et al. (2013). Technical description of version 4.5 of the Community Land Model (CLM) (Rep. NCAR/TN-503 + STR, 420).
- Pepin, N., Bradley, R. S., Diaz, H. F., Baraer, M., Caceres, E. B., Forsythe, N., et al. (2015). Elevation-dependent warming in mountain regions of the world. *Nature Climate Change*, *5*(5), 424–430. <https://doi.org/10.1038/nclimate2563>
- Pinzon, J. E., & Tucker, C. J. (2014). A non-stationary 1981–2012 AVHRR NDVI3g time series. *Remote Sensing*, *6*(8), 6929–6960. <https://doi.org/10.3390/rs608692>
- Prudhomme, C., Giuntoli, I., Robinson, E. L., Clark, D. B., Arnell, N. W., Dankers, R., et al. (2014). Hydrological droughts in the 21st century, hotspots and uncertainties from a global multimodel ensemble experiment. *Proceedings of the National Academy of Sciences of the United States of America*, *111*(9), 3262–3267. <https://doi.org/10.1073/pnas.1222473110>
- Qin, J., Yang, K., Lu, N., Chen, Y. Y., Zhao, L., & Han, M. (2013). Spatial upscaling of in-situ soil moisture measurements based on MODIS-derived apparent thermal inertia. *Remote Sensing of Environment*, *138*, 1–9. <https://doi.org/10.1016/j.rse.2013.07.003>
- Rodell, M., Houser, P., Jambor, U., Gottschalck, J., Mitchell, K., Meng, C., et al. (2004). The Global Land Data Assimilation System. *Bulletin of the American Meteorological Society*, *85*(3), 381–394. <https://doi.org/10.1175/BAMS-85-3-381>

- Sellers, P. J., Los, S. O., Tucker, C. J., Justice, C. O., Dazlich, D. A., Collatz, G. J., et al. (1996). A revised land surface parameterization (SiB2) for atmospheric GCMs. 2. The generation of global fields of terrestrial biophysical parameters from satellite data. *Journal of Climate*, 9(4), 706–737. [https://doi.org/10.1175/1520-0442\(1996\)009<0706:ARLSPF>2.0.CO;2](https://doi.org/10.1175/1520-0442(1996)009<0706:ARLSPF>2.0.CO;2)
- Su, Z., Rosnay, P., Wen, J., Wang, L., & Zeng, Y. (2013). Evaluation of ECMWF's soil moisture analyses using observations on the Tibetan plateau. *Journal of Geophysical Research: Atmospheres*, 118, 5304–5318. <https://doi.org/10.1002/jgrd.50468>
- Tian, H., Lu, C., Ciais, P., Michalak, A. M., Canadell, J. G., Saikawa, E., et al. (2016). The terrestrial biosphere as a net source of greenhouse gases to the atmosphere. *Nature*, 531(7593), 225–228. <https://doi.org/10.1038/nature16946>
- Wada, Y., Wisser, D., & Bierkens, M. F. P. (2014). Global modeling of withdrawal, allocation and consumptive use of surface water and groundwater resources. *Earth System Dynamics*, 5(1), 15–40. <https://doi.org/10.5194/esd-5-15-2014>
- Wang, L., Yuan, X., Xie, Z., Wu, P., & Li, Y. (2016). Increasing flash droughts over China during the recent global warming hiatus. *Scientific Reports*, 6(1), 30571. <https://doi.org/10.1038/srep30571>
- Wing, O. E. J., Bates, P. D., Sampson, C. C., Smith, A. M., Johnson, K. A., & Erickson, T. A. (2017). Validation of a 30 m resolution flood hazard model of the conterminous United States. *Water Resources Research*, 53, 7968–7986. <https://doi.org/10.1002/2017WR020917>
- Wood, E. F., Wood, E. F., Roundy, J. K., Troy, T. J., van Beek, L. P. H., Bierkens, M. F. P., & Blyth, E. (2011). Hyperresolution global land surface modeling: Meeting a grand challenge for monitoring Earth's terrestrial water. *Water Resources Research*, 47, W05301. <https://doi.org/10.1029/2010WR010090>
- Xu, W., Gu, S., Zhao, X. Q., Xiao, J., Tang, Y., Fang, J., et al. (2011). High positive correlation between soil temperature and NDVI from 1982 to 2006 in alpine meadow of the Three-River Source Region on the Qinghai-Tibetan plateau. *International Journal of Applied Earth Observation and Geoinformation*, 13(4), 528–535. <https://doi.org/10.1016/j.jag.2011.02.001>
- Yang, K., Koike, T., Ye, B., & Bastidas, L. (2005). Inverse analysis of the role of soil vertical heterogeneity in controlling surface soil state and energy partition. *Journal of Geophysical Research*, 110, D08101. <https://doi.org/10.1029/2004JD005500>
- Yang, K., Qin, J., Zhao, L., Chen, Y., Tang, W., Han, M., et al. (2013). A multiscale soil moisture and freeze-thaw monitoring network on the third pole. *Bulletin of the American Meteorological Society*, 94(12), 1907–1916. <https://doi.org/10.1175/BAMS-D-12-00203.1>
- Yang, K., Wu, H., Qin, J., Lin, C., Tang, W., & Chen, Y. (2014). Recent climate changes over the Tibetan plateau and their impacts on energy and water cycle: A review. *Global and Planetary Change*, 112, 79–91. <https://doi.org/10.1016/j.gloplacha.2013.12.001>
- Yuan, X., Jiao, Y., Yang, D., & Lei, H. (2018). Reconciling the attribution of changes in streamflow extremes from a hydroclimate perspective. *Water Resources Research*, 54, 3886–3895. <https://doi.org/10.1029/2018WR022714>
- Yuan, X., & Liang, X. Z. (2011). Evaluation of a conjunctive surface-subsurface process model (CSSP) over the contiguous United States at regional-local scales. *Journal of Hydrometeorology*, 12(4), 579–599. <https://doi.org/10.1175/2010JHM1302.1>
- Yuan, X., Ma, F., Wang, L., Zheng, Z., Ma, Z., Ye, A., et al. (2016). An experimental seasonal hydrological forecasting system over the Yellow River basin—Part 1: Understanding the role of initial hydrological conditions. *Hydrology and Earth System Sciences*, 20(6), 2437–2451. <https://doi.org/10.5194/hess-20-2437-2016>
- Yuan, X., Zhang, M., Wang, L., & Zhou, T. (2017). Understanding and seasonal forecasting of hydrological drought in the anthropocene. *Hydrology and Earth System Sciences*, 21(11), 5477–5492. <https://doi.org/10.5194/hess-21-5477-2017>
- Zeng, Y., Su, Z., van der Velde, R., Wang, L., Xu, K., Wang, X., et al. (2016). Blending satellite observed, model simulated, and in situ measured soil moisture over Tibetan plateau. *Remote Sensing*, 8(3), 268. <https://doi.org/10.3390/rs8030268>
- Zhang, G., Zhang, Y., Dong, J., & Xiao, X. (2013). Green-up dates in the Tibetan plateau have continuously advanced from 1982 to 2011. *Proceedings of the National Academy of Sciences of the United States of America*, 110(11), 4309–4314. <https://doi.org/10.1073/pnas.1210423110>
- Zheng, D., van der Velde, R., Su, Z., Wang, X., Wen, J., Booi, M. J., et al. (2015). Augmentations to the Noah model physics for application to the Yellow River source area. Part I: Soil water flow. *Journal of Hydrometeorology*, 16(6), 2659–2676. <https://doi.org/10.1175/JHM-D-14-0198.1>
- Zheng, D., Van Der Velde, R., Su, Z., Wen, J., & Wang, X. (2017). Assessment of Noah land surface model with various runoff parameterizations over a Tibetan River. *Journal of Geophysical Research: Atmospheres*, 122, 1488–1504. <https://doi.org/10.1002/2016JD025572>